Acta Pharmaceutica Sinica B 2026;16(2):879−899

Chinese Pharmaceutical Association
Institute of Materia Medica, Chinese Academy of Medical Sciences

Acta Pharmaceutica Sinica B

www.elsevier.com/locate/apsb
www.sciencedirect.com

ORIGINAL ARTICLE

Clostridium perfringens alpha toxin drives pathological NETosis *via* immature neutrophil mobilization and functional reprogramming

Pinnan Zhao[a,†], Zongcheng Li[c,†], Chaoyan Yao[a,d,†], Yi Zhou[e,†], Yangyihua Zhou[a], Ning Shi[a,d], Jie Wang[a], Can Xu[a], Peixun Gao[a], Xuechen Yang[a], Liang Zhang[a], Yaowei Ma[a], Jiannan Feng[a], Chunxia Qiao[a], Xinying Li[a], Changyan Li[b,*], Longlong Luo[a,*], Xiang Gao[a,*]

[a]*Academy of Military Medical Sciences, Beijing 100850, China*
[b]*Beijing Institute of Radiation Medicine, Beijing 100071, China*
[c]*State Key Laboratory of Experimental Hematology, Haihe Laboratory of Cell Ecosystem, Institute of Hematology, Department of Hematology, Fifth Medical Center, Chinese PLA General Hospital, Beijing 100071, China*
[d]*Xiangya School of Basic Medical Science, Central South University, Changsha 410078, China*
[e]*Department of Neurosurgery, The First Medical Center of Chinese PLA General Hospital, Beijing 100853, China*

Received 22 May 2025; received in revised form 7 August 2025; accepted 28 August 2025

KEY WORDS

Bacterial toxins;
Neutrophil extracellular traps;
Immature neutrophils;
Reactive oxygen species;
Single-cell transcriptomics;
Host-directed therapy;
Immunopathology;
Organ injury

Abstract *Clostridium perfringens* alpha toxin (CPA), a zinc-dependent phospholipase C, is a key virulence factor in gas gangrene. While its membrane-disrupting cytotoxicity is well characterized, its capacity to modulate neutrophil function and promote pathological inflammation is poorly defined. Here, we show that CPA induces neutrophil extracellular trap (NETs) formation by mobilizing and functionally reprogramming immature neutrophils. In a murine model, CPA challenge caused dose-dependent mortality and multi-organ injury, driven by a dramatic expansion of a pro-NETotic immature neutrophil subset identified by single-cell RNA sequencing. This was confirmed by elevated systemic NETs markers and extensive NETs deposition in damaged tissues. Mechanistically, CPA directly triggered reactive oxygen species (ROS)-dependent, peptidylarginine deiminase 4 (PAD4)-mediated NETosis in both murine and human neutrophils, revealing a conserved pathogenic mechanism. Importantly, therapeutic targeting of the NETotic pathway—*via* PAD4 inhibition, (Deoxyribonuclease I) DNase I treatment, or neutrophil

*Corresponding authors.
E-mail addresses: lichangyan@ncpsb.org.cn (Changyan Li), luolong_long@126.com (Longlong Luo), gaoxiang609@163.com (Xiang Gao).
†These authors made equal contributions to this work.

Peer review under the responsibility of Chinese Pharmaceutical Association and Institute of Materia Medica, Chinese Academy of Medical Sciences.

https://doi.org/10.1016/j.apsb.2025.09.011

depletion—significantly reduced tissue damage and improved survival. These findings identify a CPA −neutrophil−NETs axis as a central driver of immunopathology. Our study reframes CPA from a classical cytolysin to a potent immunomodulatory toxin that hijacks neutrophil fate. Our findings validate the NETotic pathway as a critical therapeutic target, providing a strong rationale for developing host-directed therapies—potentially in combination with toxin-neutralizing agents—to combat severe toxin-driven diseases.

1. Introduction

Infectious diseases remain a major cause of morbidity and mortality worldwide, especially in the context of rising antimicrobial resistance, emerging zoonotic threats, and the immunopathological consequences of severe infections[1-4]. While antibiotics have dramatically reduced mortality from bacterial infections, they are often ineffective in neutralizing secreted microbial toxins or preventing the cascade of host-mediated tissue damage driven by excessive inflammation[5-7]. This dysregulated host immune response, rather than direct pathogen-mediated damage, is increasingly recognized as the pivotal driver of organ failure in critical illnesses. A key mechanism underlying this immunopathology is the excessive formation of neutrophil extracellular traps (NETs)[8], a process strongly implicated in the progression of sepsis[9], acute respiratory distress syndrome (ARDS)[10], and severe viral infections like COVID-19[11]. In these conditions, pathogen-associated molecules, particularly bacterial toxins, can provoke a "NETosis storm" that fuels systemic inflammation, thromboinflammation, and ultimately, multi-organ injury, highlighting the urgent need for therapies that can temper this specific host response[12]. This growing recognition of host-directed pathology has shifted focus toward understanding how microbial products perturb innate immune responses and identifying adjunctive therapeutic strategies that mitigate immunopathology[13].

Clostridium perfringens is a Gram-positive, anaerobic, spore-forming bacterium capable of causing diseases ranging from foodborne illness to necrotizing soft tissue infections such as gas gangrene[14-16]. Its pathogenesis is largely mediated by over 20 identified exotoxins, among which *Clostridium perfringens* alpha toxin (CPA) is the most conserved and universally present across all toxinotypes (A−G)[17-19]. CPA is a 370-amino-acid zinc-dependent phospholipase C that hydrolyzes phosphatidylcholine and sphingomyelin in host membranes, leading to cell lysis, vascular leakage, and tissue necrosis[20,22]. Structurally, CPA contains an N-terminal catalytic domain and a C-terminal membrane-binding domain, whose coordinated action is essential for its cytotoxicity. Beyond membrane disruption, CPA activates ganglioside-Tropomyosin receptor kinase A (TrkA) signaling, promotes Reactive oxygen species (ROS) production, and triggers proinflammatory cytokine release, including IL-8[21,23,24]. In parallel, CPA and other major *Clostridium perfringens* toxins, such as CPB, ETX, and ITX, have been identified as potent activators of the NOD-like receptor protein 3 (NLRP3) inflammasome through mechanisms involving membrane damage, ionic imbalance, and oxidative stress[25-27]. While different bacterial toxins, such as staphylococcal α-hemolysin or lipopolysaccharide (LPS), are known to modulate neutrophil functions in diverse ways[28], the specific mechanisms by which CPA engages and potentially reprograms neutrophils to drive systemic pathology remain poorly defined.

Neutrophils are essential innate immune effectors that rapidly respond to infection and tissue damage[29]. In addition to phagocytosis and degranulation, they can undergo the formation of neutrophil extracellular traps (NETosis), a specialized form of cell death in which NETs-web-like DNA structures decorated with histones and granule enzymes-are expelled into the extracellular space[8,30-32]. While NETs play important roles in pathogen containment, their excessive or dysregulated formation has been implicated in a wide range of pathological conditions, including sepsis, ARDS, and thromboinflammation diseases[33,34]. For instance, the deposition of NETs in the pulmonary microvasculature is a key driver of lung injury in ARDS, while in sepsis, NETs contribute to endothelial damage and coagulopathy, leading to multi-organ failure[35,36].

Nevertheless, whether bacterial toxins such as CPA can directly induce NETosis *in vivo*, and whether they do so *via* recruitment and reprogramming of immature neutrophils, remains to be elucidated. Moreover, the extent to which these toxin-elicited NETs contribute causally to tissue damage and disease progression has not been elucidated at cellular or transcriptional resolution. These unresolved questions constrain our ability to design host-directed interventions for toxin-mediated pathologies.

In this study, we established a murine model of CPA intoxication using a structurally validated recombinant protein and performed multimodal analyses including histopathology, immune profiling, NETs quantification, and Single-cell RNA sequencing (scRNA-seq). We demonstrated that CPA induces pathological NETosis by mobilizing and reprogramming immature neutrophils, which in turn drive systemic inflammation and multi-organ injury. Pharmacological or immunological inhibition of NETs formation significantly ameliorated disease severity, highlighting the CPA-neutrophil-NETs axis as a promising target for adjunctive therapy in toxin-mediated inflammatory diseases (see Scheme 1).

2. Materials and methods

2.1. Animals

Female BALB/c mice (6−8 weeks old, 17−20 g) were obtained from Charles River Laboratories. All animals were housed under specific pathogen-free (SPF) conditions in a temperature-controlled environment (22−25 °C) with a relative humidity of 50%−60%. Standard laboratory chow and water were provided freely available. All animal experiments were approved by the Institutional Animal Care and Use Committee (IACUC) of Academy of Military Medical Sciences (IACUC-DWZX-2024-

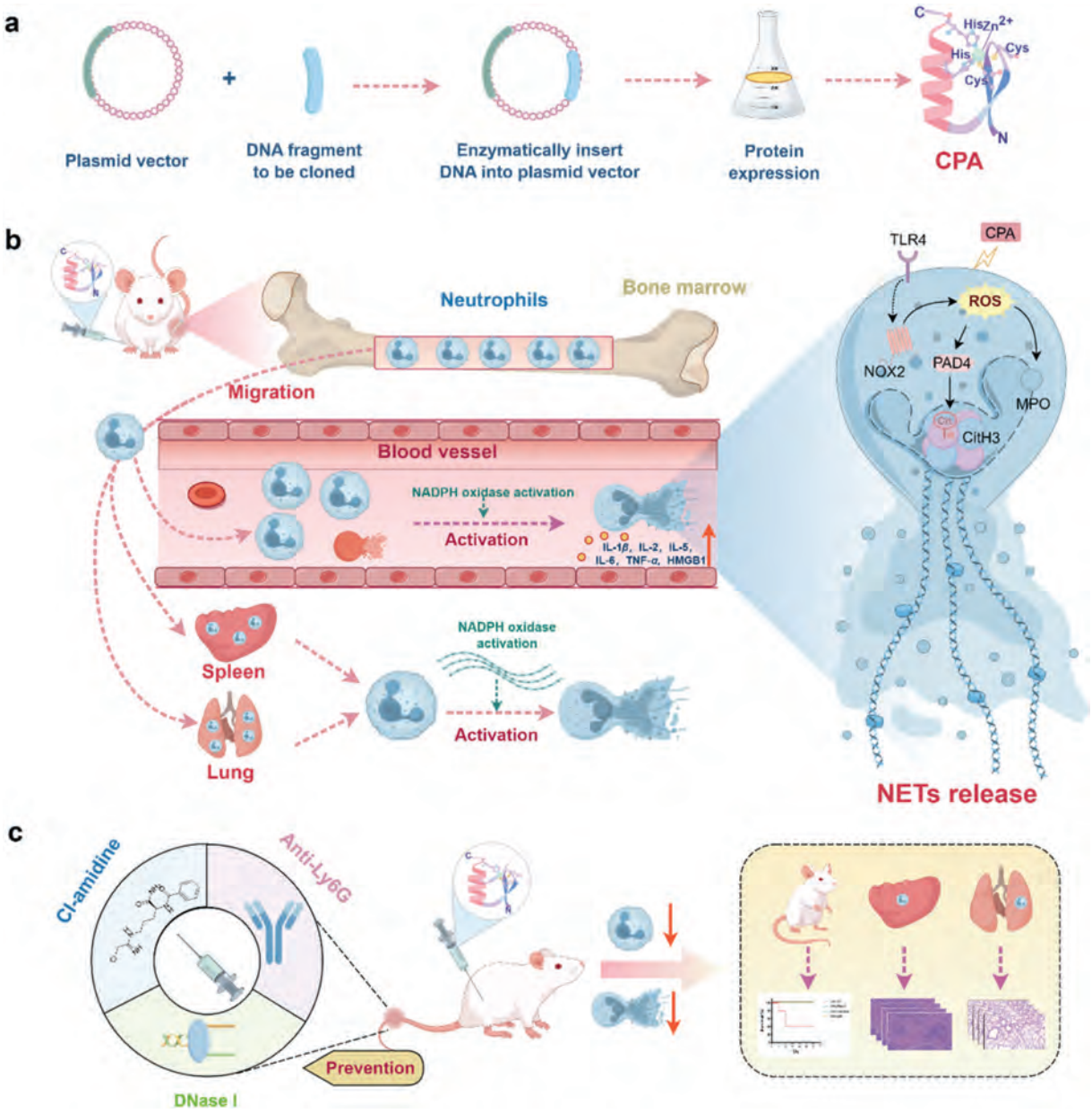

Scheme 1 *Clostridium perfringens* alpha toxin (CPA) drives the mobilization of immature neutrophils and triggers pathological NETosis, resulting in multi-organ injury. Targeting this pathway significantly mitigates tissue damage and improves survival.

621). All procedures were conducted in accordance with the Regulations for the Administration of Affairs Concerning Experimental Animals of China and the National Standard GB/T 35892-2018 for the Ethical Review of Laboratory Animal Welfare.

2.2. *Animal model of CPA challenge*

2.2.1. *CPA challenge dose exploration in mice*

To establish a CPA challenge model, mice were intraperitoneally injected with CPA at doses of 2, 10, 17.5, 20, and 25 μg/kg ($n = 6$). All procedures were performed under aseptic conditions, with each mouse receiving a 100 μL injection. The general condition of the mice, including mental status, fur appearance, appetite changes, and survival time, was monitored and recorded for up to 48 h. The dose corresponding to approximately 50% mortality was selected as the reference concentration for subsequent experiments.

2.2.2. *Organ damage and inflammatory cytokine analysis in CPA challenge*

To investigate the toxic effects of CPA challenge in mice, samples were collected at 1, 6, 12, 24 and 48 h post-treatment. Mice were anesthetized with isoflurane, and blood was obtained *via* orbital exsanguination. Following blood collection, mice were euthanized by cervical dislocation. Whole blood and serum were collected for flow cytometry and cytokine analysis. Tissue samples from the heart, liver, spleen, lungs, kidneys, stomach, and intestines were harvested, fixed in 4% paraformaldehyde, and processed for

hematoxylin and eosin (H&E) staining to assess pathological changes.

2.2.3. Immune cell analysis in CPA-challenged mice

Single-cell suspensions were prepared from peripheral blood, spleen, and bone marrow for flow cytometric analysis. Peripheral blood samples were subjected to red blood cell lysis using a commercial lysis buffer (Thermo Fisher, 00-4300-54, Waltham, MA, USA), followed by washing and surface staining. Spleen and bone marrow tissues were mechanically dissociated, filtered through a 45 μm nylon mesh, and washed with PBS to obtain single-cell suspensions.

For immune cell phenotyping in peripheral blood, cells were incubated with fluorophore-conjugated anti-mouse antibodies, including anti-CD45-PE (BioLegend, 103106, San Diego, CA, USA), anti-CD3-APC (BioLegend, 100236, San Diego, CA, USA), anti-B220-PE-Cy7 (BioLegend, 103222, San Diego, CA, USA), and anti-CD11b-eFluor 450 (BioLegend, 53-0112-82, San Diego, CA, USA), for the identification of T cells, B cells, and myeloid cells.

For immune cell subset analysis in spleen and bone marrow, additional antibody panels were used. T cell subsets were characterized using anti-CD3-APC (BioLegend), anti-CD4-BV421 (BioLegend, 100437, San Diego, CA, USA), and anti-CD8-PE-Cy7 (BioLegend, 100722, San Diego, CA, USA). Myeloid cell populations, including neutrophils and monocytes, were distinguished using anti-CD11b-eFluor 450 (Thermo Fisher, 48-0112-82, Waltham, MA, USA), anti-Ly6G-APC (BioLegend, 127614, San Diego, CA, USA), and anti-Ly6C-PE-Cy7 (BD Biosciences, 560593, New York, NY, USA). B cell and DC cell populations were analyzed using anti-CD11c-PE-Cy7 (BioLegend, 117318, San Diego, CA, USA) and anti-B220-PE (BioLegend, 103208, San Diego, CA, USA).

Following staining, cells were washed and resuspended in FACS buffer (PBS supplemented with 2% FBS) prior to acquisition. Flow cytometric data were collected using an LSRFortessa flow cytometer (BD Biosciences, X-20, New York, NY, USA) and analyzed with FlowJo software (BD Biosciences, v10.8, New York, NY, USA).

2.2.4. NETs inhibition in CPA challenge

To investigate the effects of NETs inhibition, depletion, and degradation on CPA infection, mice were intravenously injected with CI-amidine (MedChemExpress, HY-100574, Princeton, NJ, USA), anti-Ly6G (Abcam, ab238132, Cambridge, UK), and Deoxyribonuclease I (DNase I) (Sigma, D5025, St. Louis, MO, USA) *via* the tail vein.

For prophylactic intervention, mice received DNase I (65 U/day, i.v.) starting from CPA infection until the end of the experiment. Anti-Ly6G can deplete neutrophils. The day before CPA infection, mice were injected with anti-Ly6G (5 μg/g, i.v.). Subsequently, the dose was adjusted to 2.5 μg/g every other day until the experiment concluded. CI-amidine, an inhibitor of Peptidylarginine deiminase 4 (PAD4), was given 1 h before CPA infection (50 mg/kg, i.v.).

At the experimental endpoint, mice were euthanized, and samples were collected for further analysis. Lung, spleen, and kidney were fixed in 4% paraformaldehyde at 4 °C for histopathological examination and immunofluorescence analysis. Whole blood was collected *via* cardiac puncture, centrifuged at 3000 rpm for 15 min (Centrisys, CS10, Kenosha, WI, USA), and the serum was stored at −80 °C for the detection of NETs markers.

To ensure clarity, we have standardized the terminology in this study. "NETs" refers to neutrophil extracellular traps, which are the web-like structures released by neutrophils. "NETosis" refers to the process of neutrophil extracellular trap formation, representing a form of inflammatory cell death. "pro-NETotic" refers to the process of promoting the generation of NETs.

2.2.5. Single-cell analysis in CPA-challenged mice

Single-cell transcriptomic profiling was conducted to investigate peripheral immune cell responses following CPA administration. Female BALB/c mice (6−8 weeks old, 17−20 g) were used in this study. A total of six adult female mice were randomly divided into two groups ($n = 3$): a CPA-treated group and a PBS control group. Mice in the CPA group received an intraperitoneal injection of CPA at a dose of 12.5 μg/kg, while control mice were administered an equal volume of PBS.

At 12 h after treatment, peripheral blood was collected *via* cardiac puncture under sterile conditions. For each group, whole blood samples from the three mice were pooled prior to downstream processing. Red blood cells (RBCs) were lysed using ammonium-chloride-potassium lysis buffer (Thermo Fisher, A1049201, Waltham, MA, USA), and white blood cells (WBCs) were isolated. The cell pellet was resuspended in PBS containing 0.04% bovine serum albumin (BSA), filtered through a 40 μm cell strainer, and prepared as a single-cell suspension. The suspension was loaded at the recommended concentration into the Rhapsody™ HT 8-channel system (BD Biosciences, BD Rhapsody™ HT Xpress, New York, NY, USA) to generate water-in-oil emulsion droplets, each containing a single cell and a barcoded bead. Reverse transcription and cDNA amplification were carried out using the Rhapsody™ Whole Transcriptome Amplification Kit (BD Biosciences, 633801, New York, NY, USA) according to the manufacturer's instructions. The resulting libraries were sequenced on an Illumina NovaSeq 6000 platform (Illumina, NovaSeq 6000, San Diego, CA, USA) to generate high-throughput transcriptomic data.

Raw sequencing data were processed using the Cell Ranger pipeline (10 × Genomics, Cell Ranger, Pleasanton, CA, USA) for alignment to the mouse reference genome, transcript quantification, and initial cell clustering. Subsequent bioinformatic analyses, including dimensionality reduction (UMAP), clustering, and cell-type annotation, were performed using the Seurat package (Satija Lab, v4.0, New York, NY, USA) in R. Differentially expressed genes (DEGs) between the CPA and PBS groups were identified using the Wilcoxon rank-sum test with Bonferroni correction for multiple comparisons. A residual erythrocyte population due to incomplete lysis and rare epithelial cells likely originating from sample contamination were excluded from downstream analyses.

2.3. Optimized recombinant expression and purification of CPA in E. coli

To overcome challenges in CPA expression, including low yield and potential inclusion body formation as reported in previous studies, we utilized a self-constructed solubility-enhancing prokaryotic expression system. The target gene was cloned into the prokaryotic expression vector pTig-Trx (in-house constructed and laboratory-preserved) and transformed into *E. coli* TransB (DE3). This vector employs a bicistronic structure to express thioredoxin (Trx) upstream of CPA, thereby enhancing solubility and proper

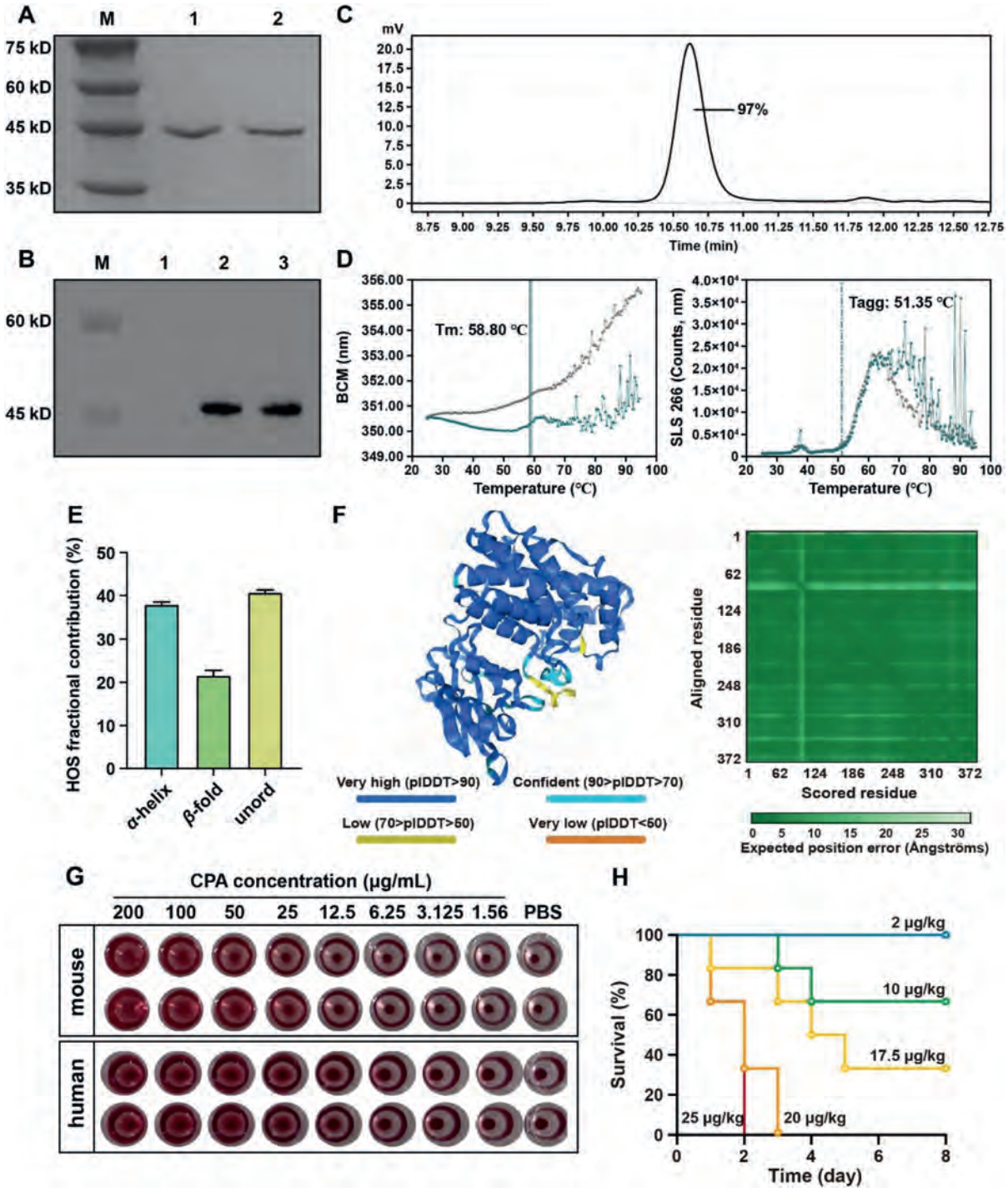

Figure 1 Expression, purification, structural characterization, and functional analysis of CPA. (A) SDS-PAGE analysis of purified CPA protein. Lane M, molecular weight marker; lanes 1 and 2, purified CPA protein, showing a distinct band at ~45 kDa. (B) Western blot analysis confirming CPA expression. Lane M, molecular weight marker; lane 1, negative control; lanes 2 and 3, purified CPA protein, confirming specific detection. (C) HPLC-SEC analysis of CPA purity. A single dominant peak accounts for >97% of the total peak area, indicating high purity. (D) Thermal stability analysis of CPA. Left, DSF curve indicating a melting temperature (T_m) of 58.80 °C. Right, SLS analysis showing an aggregation temperature (T_{agg}) of 51.35 °C. (E) Secondary structure composition of CPA determined by AQS, showing 38.48% α-helix, 20.11% β-fold and 41.41% unord regions. (F) Structural modeling of CPA using AlphaFold3. Left, predicted structural model colored by local confidence scores (pLDDT). Right, PAE plot, indicating minimal relative positional uncertainty. (G) Hemolytic activity assay of CPA on mouse and human red blood cells at different toxin concentrations. A dose-dependent hemolytic effect is observed. (H) Survival analysis of mice injected intraperitoneally with different doses of CPA. A dose-dependent lethality is observed, with 20 and 25 μg/kg causing 100% mortality, while the LD_{50} lies between 10 and 17.5 μg/kg ($n = 6$). All data are representative of at least three independent experiments. Error bars indicate mean ± SD. Statistical significance was assessed using log-rank (Mantel−Cox) test for survival analysis.

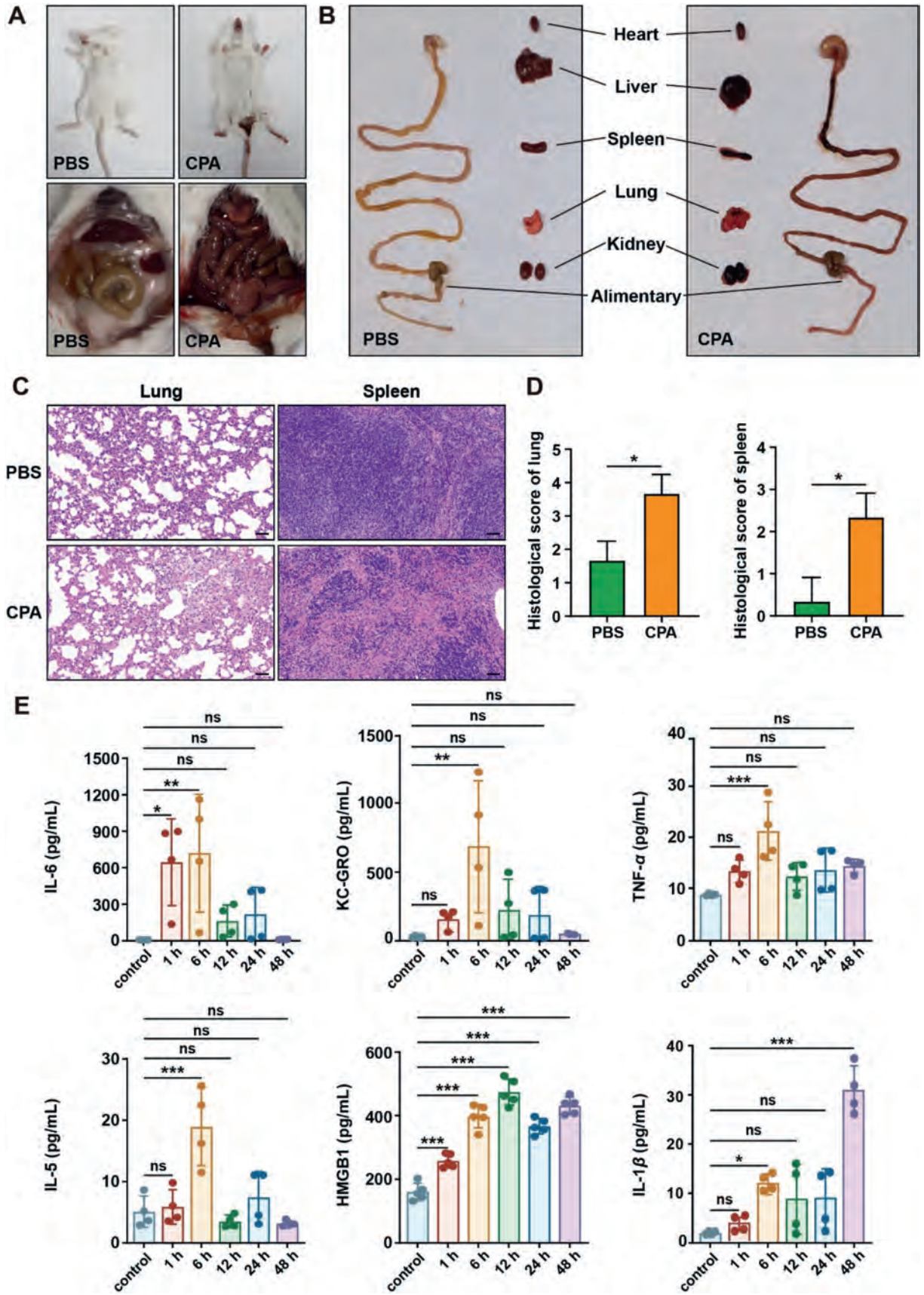

Figure 2 Target organ damage and inflammatory response in CPA-challenged mice. (A) Gross pathological examination of CPA-treated and PBS-treated mice. CPA-treated mice exhibited severe hematochezia and intra-abdominal hemorrhage, particularly in the gastrointestinal tract,

protein folding. Additionally, the TransB (DE3) strain constitutively expresses thioredoxin reductase (TrxR) and glutathione reductase (Gor), which further facilitate the production of soluble, functional CPA.

The CPA gene sequence was obtained from GenBank (ACCESSION: L43548.1) and optimized for *E. coli* expression. It was synthesized with EcoRI and XhoI restriction sites and cloned into pTig-Trx. The recombinant plasmid was transformed into TransB (DE3) and cultured in 2 YT medium (100 μg/mL ampicillin) at 37 °C, 220 rpm (Centrisys). When $OD_{600} \approx 0.8$, expression was induced with 1 mmol/L IPTG (BioLab, YT430, Beijing, China) at 16 °C for 16 h. Cells were harvested, resuspended in PBS, and lysed by sonication following freeze-thaw cycles. The soluble fraction was purified using Ni-NTA affinity chromatography, with stepwise elution (10−200 mmol/L imidazole), followed by dialysis in PBS (pH 7.4). To ensure the safety of the CPA protein sample for subsequent cell and animal experiments, the endotoxin level was measured using the Limulus Amebocyte Lysate (LAL) assay (Beyotime, ST098, Shanghai, China). According to commonly accepted safety thresholds, endotoxin levels should be below 1 EU/mL for cell-based assays and below 5 EU/mL for animal experiments. The assay was performed following the manufacturer's instructions, and a standard curve was established to ensure the accuracy of the results[37].

2.4. SDS-PAGE and Western blot analysis

Protein samples were analyzed by SDS-PAGE under reduced conditions. Following electrophoresis, the gels were stained with Coomassie Brilliant Blue (Yeasen, 20203ES10, Shanghai, China) to visualize total protein or transferred onto a nitrocellulose membrane for Western blot analysis.

For immunodetection, the membrane was blocked with 5% skimmed milk in Tris-buffered saline containing 0.1% Tween-20 (TBST) for 1 h at room temperature, followed by incubation with an HRP Anti-6 × His tag® antibody (Abcam, ab237339, Cambridge, UK) for 1 h at room temperature. The membrane was then washed three times with TBST (15 min per wash) to remove unbound antibodies. The immunoreactive bands were visualized using an ECL chemiluminescence kit (Tanon, 180-501, Shanghai, China) according to the manufacturer's instructions.

2.5. HPLC-SEC analysis of CPA purity

The purity of CPA was assessed using high-performance liquid chromatography-size exclusion chromatography (HPLC-SEC) (Thermo Fisher, 075592, Waltham, MA, USA). The protein sample (50 μL) was loaded into a pre-numbered sample tube and analyzed using a size-exclusion chromatography column. The mobile phase consisted of 150 mmol/L phosphate buffer (PB) with 5% isopropanol, and the column was equilibrated by gradually increasing the flow rate to 1 mL/min until a stable baseline was achieved. The chromatographic conditions were set as follows: a flow rate of 1 mL/min, an injection volume of 10 μL, a column temperature of 35 °C, and a detection wavelength of 280 nm, with a total acquisition time of 15 min. Data were recorded and analyzed accordingly.

2.6. Thermal stability analysis of CPA

The thermal stability of purified CPA was evaluated using differential scanning fluorimetry (DSF) and static light scattering (SLS), while its aggregation potential was assessed using dynamic light scattering (DLS). All experiments were conducted on the UNcle system (Unchained Labs, UNcle, Pleasanton, CA, USA).

For DSF and DLS assays, a temperature ramp of 1 °C/min was applied, monitoring temperature changes from 25 to 95 °C. DLS measurements were specifically conducted at 25 °C, while SLS measurements were performed at 266 and 473 nm. The melting temperature (T_m) and aggregation temperature (T_{agg}) were determined and analyzed using UNcle Analysis Software (Unchained Labs, UNcle Analysis 5.03, Pleasanton, CA, USA).

2.7. Protein secondary structure analysis

The secondary structure of CPA was analyzed using both experimental and computational approaches.

For experimental analysis, CPA was prepared at a concentration of 1 mg/mL in PBS (1 × , pH 7.4). The secondary structure was determined using microfluidic modulation spectroscopy (MMS) on the AQS-pro platform (Redshift Bio, AQS3pro, Boxborough, MA, USA) at room temperature. MMS data were collected with a modulation rate of 1 Hz and a pressure of 5 psi. The spectra were processed using delta data analysis, with normalization based on protein concentration and path length to generate higher-order structure (HOS) information. The secondary structure components (α-helix, β-sheet and unordered regions) were quantified and analyzed.

For computational structure prediction, the CPA amino acid sequence was submitted to AlphaFold3 (https://www.alphafold.ebi.ac.uk/) for *in silico* structural modeling. The predicted structure was analyzed to compare secondary structure elements with experimental data, providing additional insights into the protein's conformational stability.

24 h post-administration. (B) Dissection of major organs from CPA- and PBS-treated mice. CPA-treated mice showed dark red discoloration in multiple organs, suggestive of congestion or hemorrhage, and increased tissue sclerosis, indicative of fibrosis or necrosis. (C) Histopathological analysis of lung and spleen sections from CPA- and PBS-treated mice (H&E staining). CPA-treated lungs exhibited alveolar wall thickening, hemorrhagic areas, necrotic cell debris and granulocyte infiltration. CPA-treated spleens showed focal congestion, necrotic cell debris, and granulocyte infiltration in both red and white pulp. Scale bar = 50 μm. (D) Histopathological scoring of lung and spleen damage. CPA-treated mice exhibited significantly higher pathological scores compared with PBS controls. Data are mean ± SD, $n = 3$. Statistical significance was determined using an unpaired two-tailed *t*-test (*$P < 0.05$ *vs.* PBS-treated). (E) Serum levels of inflammatory cytokines (IL-6, KC-GRO, TNF-α, IL-5, HMGB1, and IL-1β) at different time points post-CPA administration. CPA treatment induced a significant early elevation of IL-6, KC-GRO, TNF-α, and IL-5, followed by a sustained increase in HMGB1 and a delayed surge in IL-1β. Data are mean ± SD, $n = 4$. Statistical significance was determined using one-way ANOVA followed by Tukey's multiple comparisons test (*$P < 0.05$; **$P < 0.01$; ***$P < 0.001$ *vs.* Control. ns, not significant).

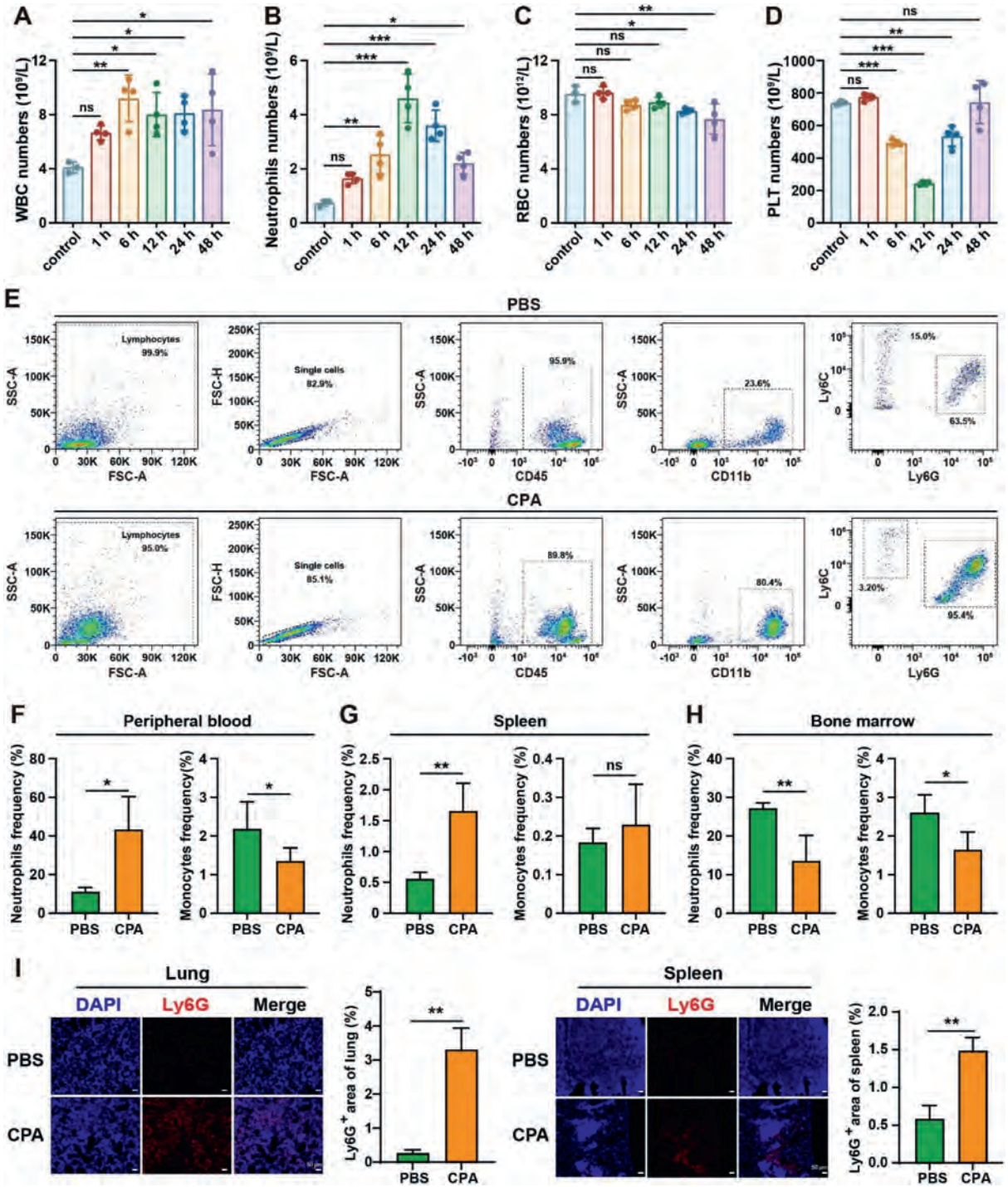

Figure 3 CPA intoxication induces systemic neutrophil mobilization and organ-specific infiltration. (A−D) CPA intoxication induces acute hematological alterations. (A) WBC counts in peripheral blood. WBC levels increased over time, peaking at 6 h and remaining elevated until 48 h. (B) Neutrophil counts in peripheral blood. Neutrophil numbers showed a rapid increase, reaching ∼10-fold of control levels at 12 h, followed by a gradual decline at 24 and 48 h. (C) RBC counts in peripheral blood. RBC levels progressively decreased from 1 h post-treatment, with a pronounced reduction at 12 h. (D) PLT counts in peripheral blood. PLT counts exhibited a biphasic response, decreasing until 12 h (∼25% of control), followed by partial recovery at 24 and 48 h. Data are mean ± SD, $n = 4$. Statistical significance was determined using one-way ANOVA followed by Tukey's multiple comparisons test (*$P < 0.05$; **$P < 0.01$; ***$P < 0.001$ *vs.* Control. ns, not significant). (E−H) Flow cytometric analysis of neutrophil and monocyte mobilization. (E) Schematic of the flow cytometry gating strategy. Neutrophils ($CD45^+CD11b^+Ly6G^+$) and monocytes ($CD45^+CD11b^+Ly6C^+$) were identified from live, single $CD45^+$ leukocytes in peripheral blood, spleen, and bone marrow. The values in the figure represent the frequency of cell relative to the cell at the upper level. (F) The frequencies of neutrophils and monocytes in the peripheral blood to the total cells. Neutrophil frequencies were significantly increased in CPA-treated mice, while monocyte levels were reduced. (G) The frequencies of neutrophil and monocyte in the spleen to the total cells. Splenic neutrophil levels were significantly elevated, whereas

2.8. Erythrocyte hemolysis assay

The hemolytic activity of CPA was evaluated using human and mouse erythrocytes. Healthy human blood samples were obtained from volunteer donors following ethical guidelines. Human and mouse RBCs were separately mixed with Alsever's Solution (Solarbio, MBS2567627, Beijing, China) at a 1:1 ratio and then washed 3−5 times with PBS to prepare a 3% RBC suspension. CPA protein was initially prepared at a starting concentration of 200 μg/mL and subjected to two-fold serial dilutions across 10 gradients. Fifty microliters of each dilution was added to a 96-well V-bottom hemagglutination plate (Solarbio, YA0590-10*1pk, Beijing, China), followed by the addition of 50 μL PBS, bringing the final reaction volume to 150 μL per well. The plate was incubated at 4 °C for 4−6 h, after which hemolysis was visually assessed and recorded.

2.9. Peripheral blood cell counts assay

To evaluate the hematological effects of CPA, peripheral blood cell counts were conducted on mice treated with a 12.5 μg/kg dose of CPA. Blood samples (10 μL per time point) were collected from the tail vein at 1, 6, 12, 24 and 48 h post-treatment. Each blood sample was immediately mixed with a pre-prepared dilution buffer to prevent coagulation. Hematological parameters were measured following the manufacturer's instructions for the hemocytometer (Mindray, BC-5385CRP, Shenzhen, China), ensuring accurate quantification of blood cell counts.

2.10. Detection of inflammatory factors

Cytokine profiling was performed using the Mesoscale Discovery (MSD) platform (MSD, Univ#K15048D-X, Rockville, MD, USA), following the manufacturer's standardized protocol. Quantitative detection was conducted on a Sector Imager 2400 system (MSD, SECTOR Imager 2400, Rockville, MD, USA), ensuring high sensitivity and accuracy. The acquired data were processed using Discovery Workbench 4.0.12 software (Ansys, 4.0.12, Canonsburg, PA, USA). Cytokine concentrations were determined by generating a standard curve and applying a four-parameter logistic (4-PL) nonlinear regression model for data analysis.

2.11. Quantification of MPO-DNA complexes, CitH3, and cell-free DNA

Serum Myeloperoxidase-DNA (MPO-DNA) complexes and Citrullinated Histone H3 (CitH3) levels were quantified using commercial enzyme-linked immunosorbent assay (ELISA) kits (MPO-DNA: Zeyou Biotechnology, YX-131615M, Tianjin, China; CitH3: BioWok, WOK-12564M1, Beijing, China) following the manufacturers' protocols. Briefly, serum samples, standards, and HRP-conjugated detection antibodies were added to microwells pre-coated with specific capture antibodies. After incubation and washing, tetramethylbenzidine (TMB) substrate was added for color development, and optical density (OD) at 450 nm was measured using a microplate reader. The concentrations of MPO-DNA complexes and CitH3 were calculated using standard curves.

Cell-free DNA (cfDNA) levels in mouse serum were measured using the Quant-iT™ PicoGreen® dsDNA Kit (Thermo Fisher, P7589, Waltham, MA, USA) according to the manufacturer's instructions. Fluorescence intensity was recorded at an excitation wavelength of 480 nm and an emission wavelength of 520 nm, and cfDNA concentrations were determined based on a standard curve[38].

2.12. Human and mouse peripheral blood neutrophil isolation, NETs induction, and molecular analysis

2.12.1. Human and mouse peripheral blood neutrophil isolation

The use of blood samples in this study complied with all relevant national regulations and institutional policies, and adhere to the principles outlined in the Declaration of Helsinki. The study was approved by the Institutional Review Board (IRB) of Beijing Institute of Pharmacology and Toxicology (Approval No: AF/SC-08/02.344), and written informed consent was obtained from all participants prior to blood collection.

Mouse peripheral blood was obtained from BALB/c mice. All procedures complied with the Regulations for the Administration of Affairs Concerning Experimental Animals of China and the National Standard GB/T 35892-2018 for the Ethical Review of Laboratory Animal Welfare.

Neutrophils were isolated from human and mouse peripheral blood using Polymorphprep™ (Serumwerk, 1895, Bernburg, Germany) and the Mouse Peripheral Blood Neutrophil Isolation Kit (Solarbio, P9201, Beijing, China), respectively, following the manufacturers' protocols. Briefly, blood samples were layered onto the Neutrophil Isolation Reagent and centrifuged at 800×*g* for 30 min at room temperature (Centrisys). The neutrophil-containing pellet was collected, resuspended in 0.9% sodium chloride, and washed by centrifugation at 400×*g* for 10 min at room temperature (Centrisys). Red blood cells were lysed using red blood cell lysis buffer (Solarbio, R1010, Beijing, China), followed by additional washing. The purified neutrophils were resuspended in RPMI-1640 medium (Gibco, 11875093, Grand Island, NY, USA) supplemented with 10% fetal bovine serum (FBS) for subsequent experiments.

2.12.2. NETs induction and collection

Isolated human and mouse neutrophils were seeded in confocal dishes or 6-well plates at a density of 2×10^6 cells/well. Cells were stimulated with 50 nmol/L phorbol 12-myristate 13-acetate (PMA) (Invivogen, 16561-29-8, Toulouse, France) for 2 h, a

monocyte levels remained unchanged. (H) The frequencies of neutrophil and monocyte in the bone marrow to the total cells. Bone marrow neutrophil levels were significantly decreased, suggesting enhanced mobilization into circulation and lymphoid organs. Data are mean ± SD, $n = 4$. Statistical significance was determined using an unpaired two-tailed *t*-test (*$P < 0.05$; **$P < 0.01$; ***$P < 0.001$ *vs.* PBS-treated. ns, not significant). (I) Neutrophil infiltration in CPA-targeted organs. Immunofluorescence staining of lung and spleen. $Ly6G^+$ neutrophils (red) and DAPI-stained nuclei (blue) were visualized in lung and spleen sections. CPA-treated mice exhibited increased neutrophil accumulation in both organs compared with PBS controls. Scale bar = 50 μm. Quantitative analysis of Ly6G in spleen and lung from mice PBS controls and CPA-treated. Data are mean ± SD, $n = 3$. Statistical significance was determined using an unpaired two-tailed *t*-test (**$P < 0.01$ *vs.* PBS-treated. ns, not significant).

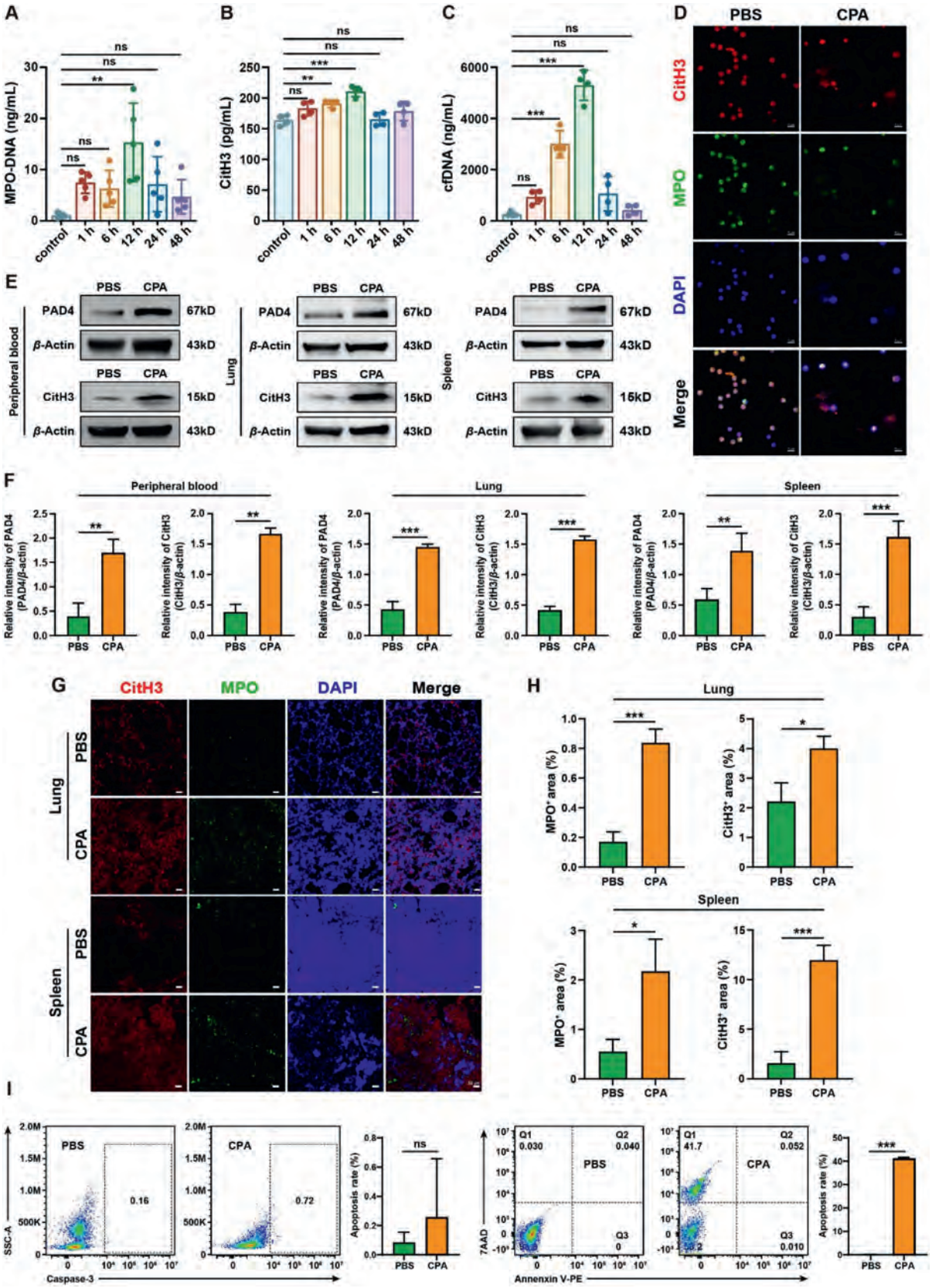

Figure 4 Elevated NETosis is observed in mice after challenged with CPA. (A–C) CPA intoxication induces an increase in NETs markers. (A) The levels of plasma MPO-DNA of PBS controls and CPA-treated at different time points were detected using ELISA. (B) The levels of plasma CitH3 of PBS controls and CPA-treated at different time points were detected using ELISA. (C) The levels of plasma cfDNA of PBS controls and CPA-treated at different time points were detected using the Picogreen method. Data are mean ± SD, $n = 4$. Statistical significance was

condition that promotes NETs formation without inducing apoptosis or necrosis.

For confocal microscopy analysis, NETs were directly used after stimulation. For Western blot analysis, supernatants were removed, and adherent NETs were washed with 2 mL cold PBS, followed by centrifugation at 1000×*g* for 10 min at 4 °C (Centrisys). The resulting pellet was collected for protein analysis.

2.12.3. Immunofluorescence and immunohistochemistry

NETs were visualized using immunofluorescence confocal microscopy. A total of 2×10^6 neutrophils were plated on poly-L-lysine (Beyotime, C0313-25 mg, Shanghai, China) precoated confocal dishes and fixed in 4% paraformaldehyde for 30 min. After blocking with immunostaining blocking solution for 30 min, cells were incubated overnight at 4 °C with primary antibodies: rabbit anti-MPO (Abcam, ab134132, Cambridge, UK) and rabbit anti-histone H3 (Abcam, ab5103, Cambridge, UK). Secondary antibody HRP-conjugated goat anti-rabbit IgG (Cell Signaling Technology, 7074S, Danvers, MA, USA) was applied, followed by staining with FITC and Cy3 fluorescent dyes, respectively. DNA was counterstained with DAPI (Beyotime, C1002, Shanghai, China).

For immunohistochemical analysis, formalin-fixed, paraffin-embedded mouse tissue sections were stained with anti-MPO (Abcam), anti-histone H3 (Abcam), and anti-Ly6G (Abcam). All samples were analyzed using laser scanning confocal microscopy.

2.12.4. Western blotting

For protein extraction, peripheral blood neutrophils, spleen, and lung tissue were lysed in RIPA buffer (Beyotime, P0013B, Shanghai, China) containing PMSF (Yeasen, 20104ES03, Shanghai, China) on ice for 30 min. Lysates were centrifuged at 12,000×*g* for 20 min at 4 °C (Centrisys), and the supernatant was collected for protein quantification. Proteins were separated using SDS-PAGE, transferred onto PVDF membranes, and blocked with 5% non-fat milk. The membranes were incubated overnight at 4 °C with rabbit anti-histone H3 (Abcam) and rabbit anti-PAD4 (Abcam, ab96758, Cambridge, UK). HRP-conjugated secondary antibodies were applied, and protein signals were detected using an ECL chemiluminescence kit (Tanon).

2.12.5. Detection of ROS assay

ROS levels were measured according to the manufacturer's instructions for the reactive oxygen detection kit (Beyotime, S0035S, Shanghai, China)[39]. A 1000-fold dilution of the 10 mmol/L DCFH-DA reagent was made using serum-free medium to create the working solution. Then, 1 mL of DCFH-DA working solution was added to 6-well plates lined with cells. Post-staining, the supernatant was aspirated, and the cells were rinsed gently three times with serum-free cell medium to eliminate any free DCFH-DA that hadn't entered the cells. The levels of ROS were measured with a BD FACS system, with detection performed in the FL1 channel (BD Biosciences, X-20, New York, NY, USA). The acquired data were subsequently processed and analyzed using FlowJo (BD Biosciences, v10.8, New York, NY, USA).

2.12.6. Cell apoptosis and caspase-3 activity assay

Cell apoptosis was measured using an Annexin V-PE/7AAD apoptosis kit (MULTISCIENCES, AT104-100, Hangzhou, China) and Cleaved Caspase-3 (Asp175) Antibody (Alexa Fluor® 488 Conjugate) (Cell Signaling Technology, 9669S, Danvers, MA, USA). Harvested neutrophils were washed with 100 μL PBS containing 2% FBS, which following incubation with 0.5 μL of PE-Annexin V and 1 μL of 7AAD or 1 μL caspase-3 antibody for 15 min at room temperature in the dark. Flow cytometric data were collected using an LSRFortessa flow cytometer (BD Biosciences, X-20, New York, NY, USA) and analyzed with FlowJo software (BD Biosciences, v10.8, New York, NY, USA).

2.12.7. Quantitative real-time polymerase chain reaction (qPCR)

The total RNA was isolated from the cell samples following the guidelines provided by the manufacturer, employing the RNAprep Pure Micro Kit (Tiangen, DP420, Beijing, China). Subsequently, complementary DNA was generated from 1 μg of the extracted RNA with the PrimeScript™ RT Master Mix (TAKARA, RR036Q, Kyoto, Japan). Quantitative PCR analysis was carried out using SYBR Green Master Mix (TAKARA, RR820A, Kyoto, Japan). For data normalization, the housekeeping gene Gapdh was used as an internal control. The corresponding primer sequences can be found in the Supporting Information section (Supporting Information Table S1).

3. Statistical analysis

All statistical analyses were performed using GraphPad Prism (GraphPad Software, version 9.0, San Diego, CA, USA). Data were assessed for normality using the Shapiro-Wilk test before further analysis. For comparisons between two groups, an unpaired Student's *t*-test was used for normally distributed data, while the Mann−Whitney U test was applied for non-normally distributed data. Comparisons among multiple groups were

determined using one-way ANOVA followed by Tukey's multiple comparisons test (**$P < 0.01$; ***$P < 0.001$ *vs.* Control. ns, not significant). (D) Representative immunofluorescence images of CitH3 and MPO in neutrophils isolated from peripheral blood of PBS controls and CPA-treated. Scale bar = 10 μm. (E) Protein levels of PAD4 and CitH3 in peripheral blood, spleen and lung from PBS controls and CPA-treated were detected using Western blot ($n = 3$). (F) Quantitative analysis of PAD4 and CitH3 in peripheral blood, spleen and lung from mice PBS controls and CPA-treated. Data are mean ± SD, $n = 3$. Statistical significance was determined using an unpaired two-tailed *t*-test (**$P < 0.01$; ***$P < 0.001$ *vs.* PBS-treated. ns, not significant). (G) Representative images demonstrating NETs presence through co-expression of CitH3 and MPO in the spleen and lung subjected to CPA treated. Scale bar = 50 μm. (H) Quantitative analysis of MPO and CitH3 in spleen and lung from mice PBS controls and CPA-treated. Data are mean ± SD, $n = 3$. Statistical significance was determined using an unpaired two-tailed *t*-test (*$P < 0.05$; ***$P < 0.001$ *vs.* PBS-treated. ns, not significant). (I) Caspase-3 activity was measured in neutrophils using a fluorometric assay. The relative Caspase-3 activity is shown, with minimal activation observed, indicating a lack of apoptosis. Flow cytometric analysis of neutrophils stained with Annexin V-PE and 7AAD. Representative dot plots show the distribution of cells in different quadrants: Q1 (Annexin V^-/$7AAD^+$), Q2 (Annexin V^+/$7AAD^+$), Q3 (Annexin V^+/$7AAD^-$), and Q4 (Annexin V^-/$7AAD^-$). The majority of neutrophils were found in Q4, indicating intact cell membranes and absence of phosphatidylserine exposure, which is inconsistent with apoptosis. Data are mean ± SD, $n = 3$. Statistical significance was determined using an unpaired two-tailed *t*-test (***$P < 0.001$ *vs.* PBS-treated. ns, not significant).

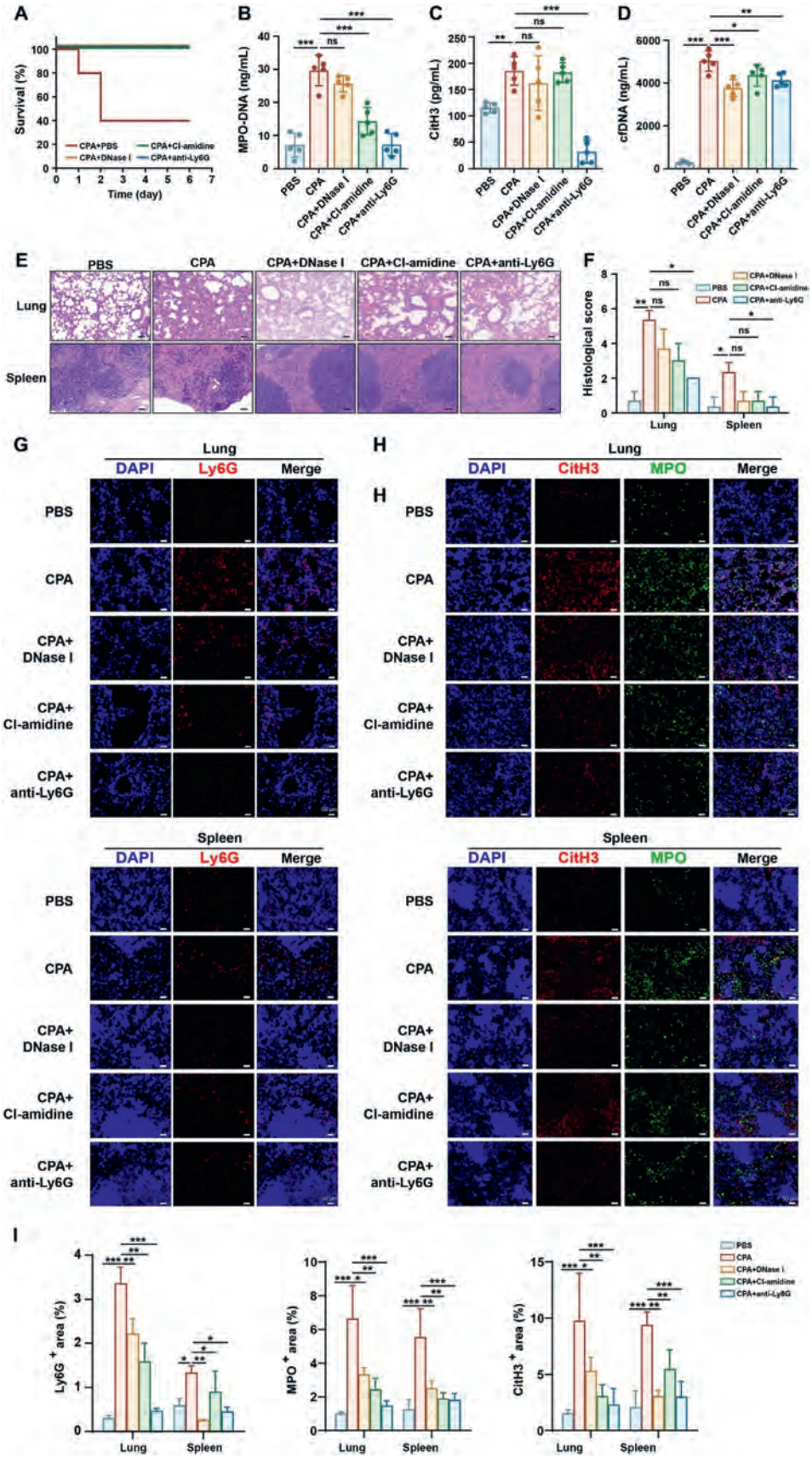

Figure 5 NETs formation inhibition, NETs degradation or NETs depletion prevent mice from CPA lethality. A mouse model of CPA-treated was established after treated with PBS, CI-amidine (inhibition of NETs formation), DNase (NETs degradation) or anti-ly6G (neutrophil

conducted using one-way analysis of variance (ANOVA), followed by Tukey's *post hoc* test for pairwise comparisons. If data did not meet normality assumptions, the Kruskal–Wallis test was used, followed by Dunn's *post hoc* test. For survival analysis, the Kaplan–Meier method was used, and differences between survival curves were assessed using the log-rank test. Results are presented as mean ± standard deviation (SD), and statistical significance was defined as $P < 0.05$.

4. Results and discussion

4.1. Expression, structural characterization, and functional analysis of CPA

To confirm the successful expression and purification of CPA, the recombinant protein was analyzed by SDS-PAGE and Western blot. A distinct band of approximately 45 kDa confirmed successful expression and high purity (Fig. 1A and B). HPLC-SEC further revealed a single dominant peak accounting for over 97% of the total area (Fig. 1C), indicating excellent purity. The endotoxin level of the CPA protein was 0.945 EU/mL, which is below the safety threshold for both cell and animal experiments (data not shown). Thermal stability analysis showed a melting temperature (Tm) of 58.80 °C and an aggregation temperature (Tagg) of 51.35 °C (Fig. 1D), suggesting moderate structural stability. Secondary structure analysis using AQS indicated that CPA comprised 38.48% α-helix, 20.11% β-sheet, and 41.41% unord regions (Fig. 1E). Structural modeling with AlphaFold3 predicted a highly confident model with a pTM score of 0.91 and most pLDDT values above 90. The predicted secondary structure (43.47% α-helix, 15.07% β-sheet, and 41.46% unord regions) was consistent with AQS results, further validating the structural fidelity of the recombinant protein (Fig. 1F). The functional activity of CPA was evaluated *in vitro* and *in vivo*. At 4 °C, CPA induced concentration-dependent hemolysis in both human and murine red blood cells. Complete hemolysis was observed at concentrations ≥25 μg/mL, characterized by a transparent red supernatant, while hemolysis was negligible below 3.125 μg/mL (Fig. 1G). *In vivo* toxicity was assessed *via* intraperitoneal injection in mice. CPA exhibited dose-dependent lethality, with 20 and 25 μg/kg doses causing 100% mortality, and the LD_{50} estimated between 10 and 17.5 μg/kg (Fig. 1H).

A critical foundation of this study was the generation of enzymatically active CPA in a soluble and structurally intact form. Traditional prokaryotic systems, such as *E. coli* BL21 or *B. subtilis*, often yield CPA as inactive inclusion bodies, with over 75% of the protein misfolded and functionally impaired. Even with refolding strategies, recovery of native activity is typically less than 20%, and inclusion body-derived CPA lacks phospholipase C activity and *in vivo* toxicity[40]. To overcome these limitations, we employed a thioredoxin-fused dual-cistronic vector system in *E. coli* TransB (DE3), which co-expresses redox enzymes to facilitate proper disulfide bond formation[41]. This strategy enabled direct production of soluble, bioactive CPA with preserved enzymatic activity and reproducible toxicity profiles, laying a robust foundation for downstream mechanistic studies.

In summary, we successfully established a robust prokaryotic expression system that yields structurally accurate and functionally active CPA. The recombinant CPA protein exhibited high purity, appropriate folding, thermal stability, hemolytic activity, and *in vivo* toxicity comparable to native toxin. These findings validate the reliability of our protein production platform and provide a critical tool for dissecting the immunopathological mechanisms of CPA in subsequent experiments.

4.2. Pathological characterization of target organ damage and systemic inflammatory cascade in CPA-intoxicated murine model

To investigate the *in vivo* toxic effects of CPA, mice were intraperitoneally injected with 25 μg/kg of recombinant CPA. Within 24 h, CPA-treated mice exhibited overt signs of gastrointestinal injury, including hematochezia and reduced mobility (Fig. 2A). Postmortem examination revealed extensive intra-abdominal hemorrhage, with the gastrointestinal tract being the most prominently affected. Gross pathological inspection of major organs revealed marked discoloration and tissue sclerosis in CPA-treated mice, particularly in the spleen and lung, suggestive of hemorrhage, inflammation, and possible necrosis (Fig. 2B).

Histological analysis further confirmed organ-specific damage. The lung and spleen exhibited the most significant pathological alterations, including alveolar wall thickening, septal edema, granulocyte infiltration, and focal hemorrhage in the lungs, as well as red pulp congestion and necrotic debris in the spleen (Fig. 2C). Quantitative histopathological scoring corroborated these findings, with the spleen and lungs showing statistically significant tissue damage compared to controls (Fig. 2D). In contrast, the heart, liver, stomach, and intestine displayed minimal or no observable pathology, while the kidney showed only mild tubular changes (Supporting Information Fig. S1).

These results suggest that CPA preferentially targets immune-rich organs such as the spleen and lungs, which are critical hubs for systemic inflammatory regulation. The observed pulmonary pathology-characterized by vascular leakage, neutrophil infiltration, and alveolar collapse-is reminiscent of acute lung injury (ALI) or early-stage ARDS, conditions often associated with dysregulated neutrophil activity and excessive cytokine release[42,43]. Similarly, damage to the spleen may compromise host immune homeostasis, exacerbating systemic inflammation.

To further characterize the systemic inflammatory response triggered by CPA, we profiled serum concentrations of 10

depletion). (A) Survival analysis of mice after NETs inhibitor prophylaxis before CPA treated. Three different NETs inhibitors were effective in improving the survival rate of mice ($n = 6$). (B) The MPO-DNA levels in plasma were detected in the mouse model. (C) The CitH3 levels in plasma were detected in the mouse model. (D) The cfDNA levels in plasma were detected in the mouse model. Data are mean ± SD, $n = 5$. Statistical significance was determined using one-way ANOVA followed by Tukey's multiple comparisons test (*$P < 0.05$; **$P < 0.01$; ***$P < 0.001$ *vs.* CPA-treated. ns, not significant). (E) Paraffin-embedded mouse spleen and lung tissue samples were stained with H&E. Representative histological images are shown at 200× magnification. Scale bar = 50 μm. (F) Histopathological changes in the spleen and lung of mice were evaluated using histological scores. Data are mean ± SD, $n = 3$. Statistical significance was determined using an unpaired two-tailed *t*-test (*$P < 0.05$; **$P < 0.01$ *vs.* CPA-treated. ns, not significant). (G) Representative immunofluorescence images of Ly6G in spleen and lung in the mouse model are present. Scale bar = 50 μm. (H) Representative images demonstrating NETs presence through co-expression of CitH3 and MPO in the spleen and lung in the mouse model. Scale bar = 50 μm.

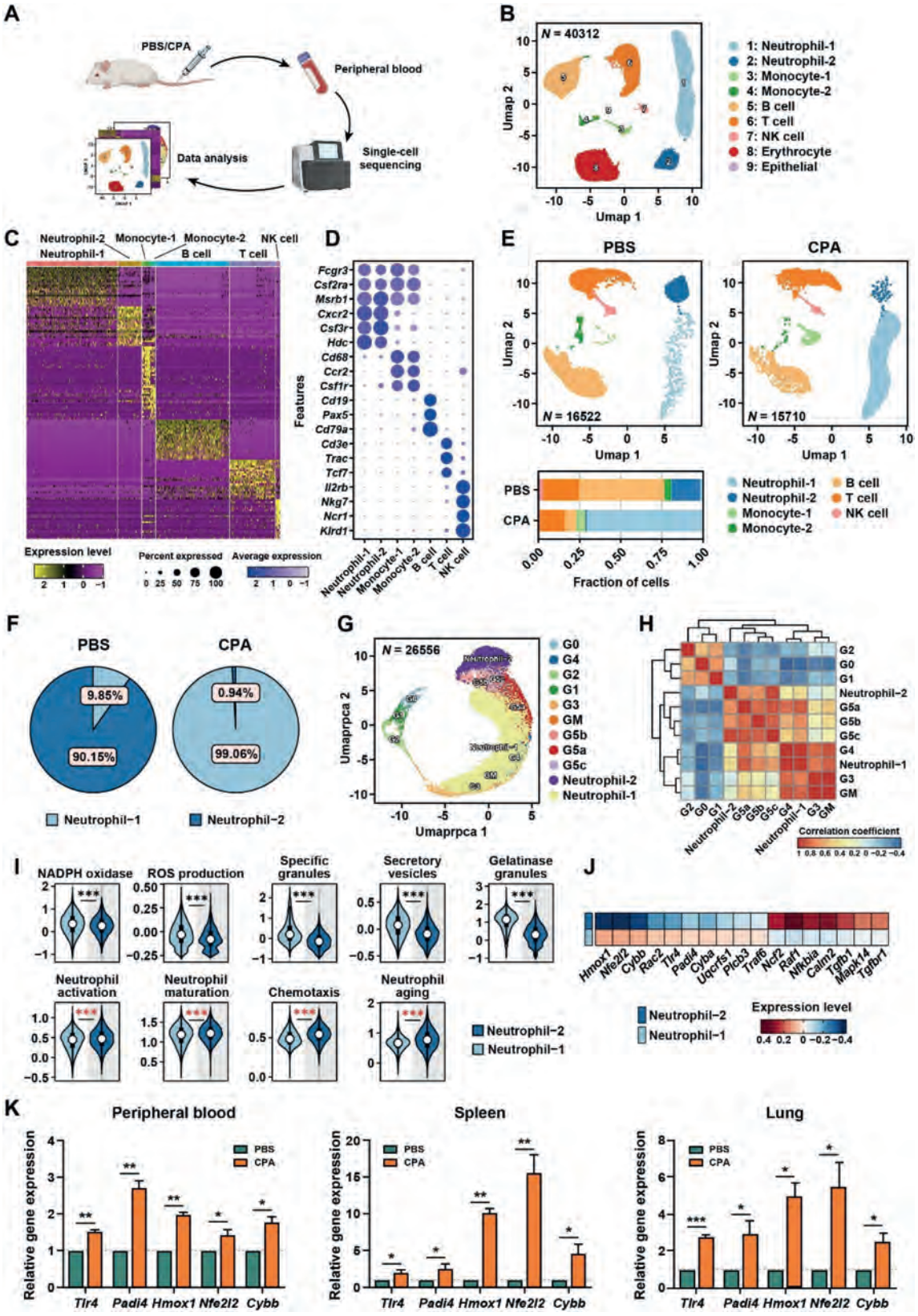

Figure 6 Single-cell transcriptomic profiling reveals CPA-induced neutrophil expansion and functional reprogramming in peripheral blood. (A) Schematic overview of the experimental workflow. Peripheral blood mononuclear cells (PBMCs) from CPA- and PBS-treated mice were subjected to scRNA-seq for immune profiling. (B) UMAP visualization identified nine distinct cell clusters, including four myeloid subsets (immature and mature neutrophils: Neutrophil-1 and Neutrophil-2; monocytes: Mono-1 and Mono-2), three lymphoid subsets (B cells, T cells, NK cells), as well as erythroid and epithelial populations. Each dot represents one cell, color-coded by cluster identity. (C) Heatmap illustrating differential gene

cytokines at multiple time points post-injection (1, 6, 12, 24 and 48 h). Among these, IL-6, KC-GRO, TNF-α, IL-5, HMGB1, and IL-1β displayed dynamic and significant alterations, while IL-10, IL-2, IFN-γ, and IL-12p70 showed relatively insignificant alterations (Fig. 2E, Supporting Information Fig. S2). IL-6 and TNF-α exhibited early and robust elevation, peaking at 1−6 h, consistent with their roles as first-wave cytokines in acute inflammatory responses. KC-GRO served as the principal chemokine for neutrophil recruitment. A rapid upregulation within 6 h signified the onset of acute inflammation and was strongly associated with neutrophil chemotaxis and infiltration. The transient increase in IL-5 may reflect early eosinophil activation. HMGB1, a late-phase damage-associated molecular pattern (DAMP), increased steadily and remained elevated beyond 24 h, suggesting ongoing cellular injury and secondary immune activation[44-46]. Strikingly, IL-1β levels surged dramatically at 48 h, indicating a delayed but strong activation of inflammasome-mediated pathways. These cytokine dynamics reflect a biphasic inflammatory response induced by CPA: an early cytokine storm driven by IL-6 and TNF-α, followed by sustained tissue damage and inflammasome activation marked by HMGB1 and IL-1β.

Taken together, these data demonstrate that CPA induces severe multi-organ pathology *in vivo*, with the spleen and lung as primary targets. The associated cytokine profile reveals a complex, time-dependent inflammatory cascade that likely contributes to tissue damage and mortality. These findings support the hypothesis that CPA acts not merely as a cytolytic agent, but as a potent immunopathogenic trigger capable of orchestrating a systemic inflammatory response. This expands the current understanding of CPA-mediated pathogenesis and highlights its potential relevance as a model toxin for studying inflammation-driven organ failure.

4.3. CPA intoxication induces systemic neutrophil mobilization and organ-specific infiltration

To evaluate the hematological and innate immune response to CPA intoxication, we performed peripheral blood analysis, immune cell profiling *via* flow cytometry, and tissue-level neutrophil infiltration assays in mice.

CPA-treated mice exhibited marked alterations in peripheral blood parameters (Fig. 3A−D). WBC counts increased progressively after CPA administration, peaking at 6 h (∼2-fold *vs.* control, $P < 0.05$) and remaining elevated through 48 h (Fig. 3A). Among leukocyte subsets, neutrophils showed the most prominent response, with a ∼10-fold increase at 12 h ($P < 0.001$), followed by a gradual decline during the late phase (Fig. 3B). In parallel, RBC counts decreased significantly from 1 h post-injection, with a pronounced drop at 12 h and continued decline at 48 h (Fig. 3C), possibly due to CPA-induced hemolysis. Platelet (PLT) counts exhibited a biphasic pattern, declining until 12 h (∼25% of control, $P < 0.001$), followed by partial recovery by 48 h (Fig. 3D). These results indicate that CPA intoxication triggers acute hematological stress, characterized by neutrophilia, anemia, and thrombocytopenia—hallmarks of systemic inflammatory activation.

To further dissect the immune response dynamics, we analyzed neutrophil distribution across bone marrow, peripheral blood, and spleen using flow cytometry (Fig. 3E). CPA-treated mice exhibited a significant reduction in bone marrow neutrophils (−16.35%, $P < 0.01$), accompanied by increased circulating neutrophils (+32.20%, $P < 0.05$) and splenic neutrophils (+1.1%, $P < 0.01$) (Fig. 3F−H). In contrast, other immune subsets, including T cells, B cells, DC cells, and monocytes, remained largely unchanged (Supporting Information Figs. S3 and S4). These findings suggest that CPA-induced inflammation is predominantly neutrophil-driven, involving rapid bone marrow egress and redistribution to peripheral compartments.

To assess whether systemic neutrophilia leads to tissue-level infiltration, we performed immunofluorescence staining for Ly6G, a neutrophil-specific marker. CPA-treated mice exhibited significant $Ly6G^+$ neutrophil accumulation in both the lung and spleen compared with PBS controls (Fig. 3I). In the lung, neutrophils were distributed around inflamed alveolar regions, consistent with histological findings of alveolar wall thickening and hemorrhage. In the spleen, $Ly6G^+$ cells were widely distributed in both red and white pulp, indicating activation of the splenic immune niche.

This mobilization pattern is reminiscent of "emergency granulopoiesis," a compensatory hematopoietic response commonly observed during acute infections, sepsis, or trauma[47,48]. However, unlike canonical models such as LPS-induced endotoxemia—where neutrophilia is pronounced but largely confined to circulation—CPA exposure resulted in organ-specific redistribution, particularly to the spleen and lung, suggesting a distinctive trafficking pattern. These organ-level infiltration patterns are notably distinct from those reported in response to other bacterial toxins. For instance, *Staphylococcus aureus* α-toxin and Panton−Valentine leukocidin (PVL) typically induce neutrophil lysis and localized NETs formation at infection sites, but do not elicit widespread systemic redistribution[49]. In contrast, CPA appears to act not only as a local cytolytic agent but also as a systemic immunomodulator, promoting neutrophil mobilization and tissue-specific infiltration. The preferential accumulation of neutrophils in immune-rich organs such as the spleen may further amplify the inflammatory cascade through local cytokine release

expression patterns across identified immune cell subsets. (D) Bubble plot of canonical marker genes across cell types. Bubble size reflects the proportion of expressing cells; color intensity indicates mean expression levels. (E) CPA challenge induced a profound shift in immune cell composition, with neutrophils becoming the predominant population. The proportion of immature Neutrophil-1 cells increased from 2.83% to 97.17%, while mature Neutrophil-2 cells decreased from 96.34% to 2.66%. (F) Pie chart of population proportions of neutrophils under PBS and CPA treatment conditions. (G) UMAP projection aligned Neutrophil-1 cells with immature bone marrow-derived G3/4 neutrophils, whereas Neutrophil-2 resembled mature G5a/b/c subsets, indicating CPA-induced mobilization of immature neutrophils. (H) Heatmap showing transcriptional similarity between neutrophil subsets and established maturation stages. (I) Violin plots comparing gene module scores between Neutrophil-1 and Neutrophil-2. Neutrophil-1 displayed significantly higher scores for NADPH oxidase and ROS production pathways, both critical for NETs formation (***$P < 0.001$). (J) Heatmap of key NETs-related genes. Neutrophil-1 cells highly expressed *Tlr4*, *Hmox1*, *Cybb*, *Padi4*, and *Nfe2l2*, suggesting enhanced oxidative and mitochondrial activity supporting NETs release. (K) qPCR analysis of *Tlr4*, *Padi4*, *Hmox1*, *Nfe2l2*, and *Cybb* mRNA expression in PBMCs, bulk spleen tissue, and bulk kidney tissue from mice 12 h post-treatment of CPA. Data are mean ± SD, $n = 3$. Statistical significance was determined using an unpaired two-tailed *t*-test (*$P < 0.05$; **$P < 0.01$; ***$P < 0.001$ *vs.* PBS-treated. ns, not significant).

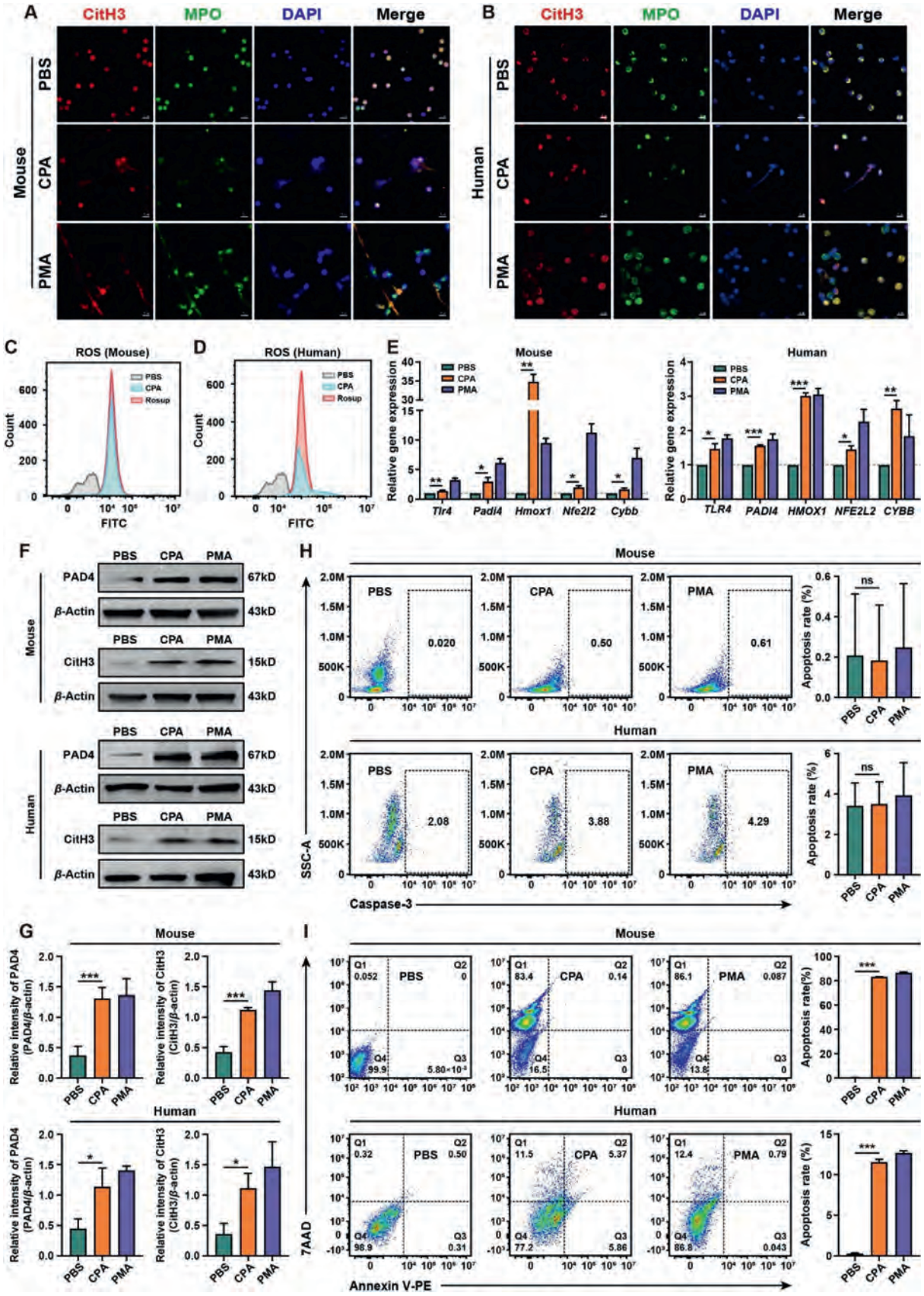

Figure 7 CPA directly induces NETosis in both murine and human neutrophils *in vitro*. (A) Representative immunofluorescence images of purified neutrophils from mice stimulated *in vitro* with PBS, CPA, or PMA (positive control). Cells were stained for CitH3 (red) and MPO (green). Scale bar = 10 μm. (B) Representative immunofluorescence images of purified neutrophils from humans stimulated *in vitro* with PBS, CPA, or

and cellular interaction, contributing to the observed organ damage.

To our knowledge, this is the first study to comprehensively characterize CPA-induced neutrophil dynamics across hematopoietic and peripheral compartments, linking these changes to tissue-level damage and systemic inflammation. The temporal coincidence of peak neutrophilia (12 h) with maximal cytokine release and histopathological injury supports the hypothesis that neutrophil activation and migration are not merely secondary to CPA toxicity, but central to its inflammatory pathogenesis. These findings reveal a novel immunopathological role for CPA beyond its classical cytolytic function, providing mechanistic insight into its contribution to toxin-mediated organ injury.

4.4. CPA exposure leads to increased NETs formation

In the process of pathogen infection, the abnormal increase of neutrophils is often accompanied by the production of pathological NETs. To evaluate whether CPA intoxication triggers NETs formation, we quantified three canonical NETs-associated markers in serum at multiple time points following CPA administration (1, 6, 12, 24, and 48 h), including MPO−DNA complexes, CitH3, and cfDNA. CPA exposure led to a significant, time-dependent increase in all three markers (Fig. 4A−C). MPO−DNA levels rose steadily, peaking at 12 h (1.03 *vs.* 15.31 ng/mL, $P < 0.01$), and declined thereafter. CitH3 followed a similar trajectory, reaching maximal levels at 12 h (163.7 *vs.* 210.53 pg/mL, $P < 0.001$). cfDNA exhibited a sharp surge: after a modest rise at 6 h, it increased ∼25-fold at 12 h (258.61 *vs.* 5295.6 ng/mL, $P < 0.001$), followed by rapid normalization.

The temporal kinetics of these NETs markers closely paralleled the observed neutrophil mobilization (Fig. 3B), supporting the hypothesis that CPA-induced neutrophil activation culminates in NETs release. This is consistent with previous reports showing that excessive neutrophil activation by microbial stimuli or sterile inflammation can trigger NETosis, contributing to tissue injury and immune dysregulation[50]. As Fig. 4D shown, CPA challenge resulted in the release of NETs from neutrophils in peripheral blood of mice., which displayed robust co-localization of MPO and CitH3 (Fig. 4D). Since PAD4-mediated histone citrullination is essential for chromatin decondensation during NETosis, we next examined PAD4 and CitH3 expression in target tissues. Western blot analysis revealed significant upregulation of both proteins in lung and spleen tissues following CPA exposure (Fig. 4E and F). To confirm that extracellular DNA originated from NETs in target tissues, we performed immunofluorescence staining for MPO and CitH3 in spleen and lung. The enhanced MPO-CitH3 co-localization was observed (Fig. 4G and H), spatially aligned with regions of inflammation and tissue injury (Figs. 2D and 3I). We next sought to rule out classical apoptosis as the primary mechanism of CPA-induced neutrophil death. Consistent with a non-apoptotic pathway, CPA did not trigger significant Caspase-3 activation. This was further substantiated by Annexin V/7-AAD flow cytometry, which revealed that CPA-treated neutrophils did not progress through a canonical early apoptotic stage (Annexin V^+/7-AAD^-) (Fig. 4I). The absence of these key apoptotic signatures provides strong evidence that CPA preferentially drives neutrophils toward NETosis rather than apoptosis.

These findings collectively demonstrate that CPA intoxication induces robust NETs formation both systemically and within injured organs. Notably, the spatial overlap between NETs formation and tissue damage suggests a causative link, wherein CPA-induced NETosis may actively contribute to organ injury. Compared to other bacterial toxins, CPA appears to be a particularly potent inducer of NETs. While LPS and *Staphylococcus aureus* α-toxin have been shown to stimulate NETosis *in vitro* or at localized infection sites, they rarely elicit sustained NETs formation in distal organs[51]. Similarly, PVL induces rapid neutrophil lysis rather than classical NETosis, which is achieved through Ca^{2+}-activated SK channels and myeloperoxidase activity[49]. In contrast, CPA promotes both systemic neutrophil mobilization and PAD4-dependent NETs generation across multiple compartments, indicating a broader immunopathological footprint.

Our study demonstrates for the first time that CPA not only activates neutrophils but also drives widespread NETs formation *in vivo*. These findings expand our understanding of CPA as not merely a cytolytic toxin, but as a potent immunomodulator capable of orchestrating innate immune effector mechanisms such as NETosis. Given the established role of NETs in promoting vascular leakage, endothelial damage, and thrombosis[52,53], targeting CPA-induced NETs may represent a novel therapeutic strategy to mitigate toxin-mediated tissue injury.

4.5. Targeting NETs ameliorates CPA-induced inflammation and organ injury

To determine the functional role of NETs in CPA-induced pathology, we investigated whether pharmacological inhibition, enzymatic degradation, or cellular depletion of NETs components could alleviate systemic inflammation and organ injury. Three

PMA (positive control). Cells were stained for CitH3 (red) and MPO (green). Scale bar = 10 μm. (C) Flow cytometric analysis of intracellular ROS production in mice PBMCs stimulated *in vitro* with PBS, CPA, or Rosup (positive control). Histograms show DCFH-DA fluorescence within the gated neutrophil population. (D) Flow cytometric analysis of intracellular ROS production in human PBMCs stimulated *in vitro*. Histograms show DCFH-DA fluorescence within the gated neutrophil population. (E) Relative mRNA expression of NETs-associated genes in stimulated mice PBMCs (*Tlr4*, *Padi4*, *Hmox1*, *Nfe2l2*, and *Cybb*) and human PBMCs (*TLR4*, *PADI4*, *HMOX1*, *NFE2L2*, and *CYBB*), as determined by qPCR. Data are mean ± SD, $n = 3$. Statistical significance was determined using one-way ANOVA followed by Tukey's multiple comparisons test (*$P < 0.05$; **$P < 0.01$; ***$P < 0.001$ *vs.* PBS-treated. ns, not significant). (F) Representative Western blot detecting PAD4 and CitH3 protein levels in lysates from stimulated mice PBMCs and human PBMCs ($n = 3$). (G) Densitometric quantification of the protein bands shown in (F). Data are mean ± SD, $n = 3$. Statistical significance was determined using one-way ANOVA followed by Tukey's multiple comparisons test (*$P < 0.05$; ***$P < 0.001$ *vs.* PBS-treated. ns, not significant). (H) Caspase-3 activity measured by flow cytometry within the gated neutrophil population of stimulated mice PBMCs and human PBMCs. Data are mean ± SD, $n = 3$. Statistical significance was determined using an unpaired two-tailed *t*-test (*vs.* PBS-treated. ns, not significant). (I) Flow cytometric analysis of apoptosis in stimulated mice PBMCs and human PBMCs using Annexin V and 7-AAD staining. Representative dot plots are shown. The bar graph shows the quantification of the live cell percentage (Annexin V^-/7-AAD^-) within the gated neutrophil population. Data are mean ± SD, $n = 3$. Statistical significance was determined using an unpaired two-tailed *t*-test (***$P < 0.001$ *vs.* PBS-treated. ns, not significant).

established strategies were employed: (1) inhibition of PAD4-a key enzyme mediating histone citrullination and chromatin decondensation—using Cl-amidine; (2) enzymatic degradation of extracellular chromatin using DNase I; and (3) depletion of neutrophils *via* anti-Ly6G monoclonal antibody.

Survival analysis revealed that all three interventions significantly improved outcomes in CPA-challenged mice, with 100% survival in each pre-treated group compared to 40% in untreated controls ($P < 0.05$; Fig. 5A). These findings support a causal role for NETs in CPA-induced lethality and suggest that both formation and persistence of NETs are critical to disease progression.

We first assessed the impact of these interventions on NETs production, as measured by serum levels of MPO−DNA complexes, CitH3, and cfDNA (Fig. 5B−D). DNase I significantly decreased cfDNA ($P < 0.001$) but did not alter MPO−DNA or CitH3 levels, consistent with its mechanism of degrading, rather than preventing, NETs release. Anti-Ly6G treatment led to a profound reduction in both MPO−DNA and CitH3 levels ($P < 0.05$), in some cases below baseline, reflecting robust depletion of NETs-producing neutrophils; however, cfDNA levels remained unchanged. In contrast, Cl-amidine significantly reduced MPO−DNA levels ($P < 0.001$), indicating effective suppression of NETs formation, while its effects on CitH3 and cfDNA were minimal. Histological analysis confirmed that NETs-targeted interventions alleviated CPA-induced tissue injury (Fig. 5E and F). Pulmonary vascular congestion, alveolar septal thickening, and neutrophil infiltration were substantially reduced. In the spleen, lymphocyte necrosis and splenic architectural disruption were ameliorated. Among the strategies, anti-Ly6G conferred the greatest protective effect, followed by DNase I and Cl-amidine. Immunofluorescence staining further demonstrated reduced neutrophil accumulation and NETs deposition (MPO-CitH3 co-localization) in lung and spleen tissues across all treatment groups (Fig. 5G−I), correlating with decreased inflammation and histopathological damage.

These results establish NETs as key pathogenic mediators of CPA-induced systemic inflammation and organ dysfunction. Importantly, the distinct mechanisms of the three therapeutic strategies reveal complementary intervention points: Cl-amidine interferes with NETosis initiation; DNase I accelerates extracellular DNA clearance; and anti-Ly6G eliminates the cellular source of NETs. Comparable approaches have shown efficacy in models of sepsis, ARDS, and sterile inflammation[38], underscoring the translational potential of NETs-targeted therapies in toxin-mediated diseases. In addition, the CitH3 neutralizing antibodies demonstrate significant therapeutic potential in thrombotic, inflammatory and infectious diseases by targeting the core components of NETs. After binding to CitH3, the antibodies inhibit its interaction with DNA, reducing the release of NETs (for example, it can lower the thrombus load in the acute cerebral infarction model). In the malaria model, the CitH3 neutralizing antibodies significantly reduced the incidence of acute lung injury, which was associated with a decrease in angiopoietin-2 levels[54].

Nevertheless, further optimization of these strategies is essential for clinical translation. For example, Ly6G is a neutrophil-specific marker in mice but has no human homolog, limiting direct translational application. Human-compatible targets such as CD66b or CD177 may offer more precise neutrophil depletion strategies[55]. Similarly, while Cl-amidine and DNase I demonstrate efficacy in murine models, their pharmacokinetics, tissue distribution, stability, and potential off-target effects require comprehensive evaluation[56,57]. Ultimately, future studies should aim to develop next-generation NETs modulators that selectively block NETs-mediated tissue injury without compromising host defense, or combine NETs inhibition with CPA-neutralizing agents to achieve synergistic protection. Such efforts will help translate our mechanistic insights into clinically viable interventions for toxin-induced inflammatory diseases.

4.6. ScRNA-seq reveals CPA-induced neutrophil mobilization and functional reprogramming

To gain comprehensive insight into the immunological impact of CPA exposure, we performed scRNA-seq on peripheral blood mononuclear cells (PBMCs) collected from CPA-treated and control mice (Fig. 6A). Unsupervised clustering and canonical marker analysis identified major hematopoietic lineages, including four myeloid subsets (two neutrophil and two monocyte clusters) and three lymphoid populations (B cells, T cells, and NK cells) (Fig. 6B−D).

CPA exposure induced a profound shift in peripheral immune cell composition. In control mice, lymphocytes (particularly B and T cells) dominated the PBMC pool. However, following CPA challenge, neutrophils became the predominant population, increasing from 19% to 71% (Fig. 6E), consistent with our flow cytometry data (Fig. 3F). This observation underscores the dominance of innate immune responses in CPA-induced systemic inflammation.

Further analysis revealed two transcriptionally distinct neutrophil subsets, designated Neutrophil-1 and Neutrophil-2 (Fig. 6C). Under physiological conditions, Neutrophil-2 dominated the peripheral pool and expressed gene signatures consistent with mature G5a/b/c granulocytes. In contrast, CPA-treated mice displayed a near-complete replacement of circulating neutrophils by Neutrophil-1, which expanded to 99% of the neutrophil compartment (Fig. 6F). Reference-based annotation using published neutrophil atlases identified Neutrophil-1 as an immature G3/4-like population normally restricted to the bone marrow (Fig. 6G and H)[58,59]. Cell cycle analysis revealed no evidence of proliferation (Supporting Information Fig. S5), further suggesting that Neutrophil-1 accumulation resulted from bone marrow egress rather than peripheral proliferation. CPA thus appears to trigger a state of emergency granulopoiesis, mobilizing immature neutrophils into the bloodstream.

To further investigate the functional divergence between Neutrophil-1 and Neutrophil-2 following CPA exposure, we analyzed their transcriptional profiles in detail. Neutrophil-1 exhibited significantly higher module scores for NADPH oxidase activity, ROS production, and granule content—including specific granules, gelatinase granules, and secretory vesicles—suggesting enhanced effector readiness (Fig. 6I). In addition, Neutrophil-1 showed elevated activation and aging scores but reduced chemotaxis and maturation signatures, consistent with a systemically mobilized, immature, yet functionally activated neutrophil phenotype.

At the gene level, Neutrophil-1 demonstrated robust upregulation of a coordinated set of genes that constitute a functional axis for NETosis, linking pathogen sensing (*Tlr4*), NADPH oxidase-mediated ROS production (*Cybb*/NOX2), and chromatin remodeling (*Padi4*), alongside a coupled oxidative stress response (*Nfe2l2*/*Hmox1*) (Fig. 6J).

Tlr4 mediates inflammatory signaling and can activate NOX2 *via* MyD88/TRIF pathways[60]; *Cybb* encodes the catalytic subunit of the NOX2 complex that directly generates superoxide

radicals[61]; *Padi4* catalyzes histone citrullination, facilitating chromatin decondensation and NETs release[62]; *Nfe2l2* and its downstream target *Hmox1* coordinate the cellular antioxidant response to ROS[63]. The convergence of these genes in Neutrophil-1 suggests that this subset is transcriptionally primed for NETosis and oxidative effector responses.

To determine if the pro-NETotic transcriptional program identified in Neutrophil-1 corresponded to a broader inflammatory response in key target organs, we performed qPCR on bulk tissue from the spleen and kidney, as well as on circulating PBMCs, 12 h after CPA challenge. Consistent with the induction of a systemic inflammatory state, CPA treatment led to a significant upregulation of the pro-inflammatory and oxidative stress-related genes (*Tlr4, Padi4, Hmox1, Nfe2l2, and Cybb*) in both the spleen and kidney (Fig. 6K). Collectively, these qPCR results demonstrate that CPA intoxication triggers a robust, tissue-wide upregulation of genes associated with the NETosis machinery and oxidative stress. This creates a pro-inflammatory environment in target organs that is consistent with, and likely driven in part by, the specialized neutrophil subset identified in our single-cell analysis.

Together, these findings indicate that CPA induces rapid mobilization of transcriptionally reprogrammed, immature neutrophils from the bone marrow into peripheral tissues. This subset, defined as Neutrophil-1, is primed for NETs formation through coordinated upregulation of ROS-generating and chromatin-modifying genes, suggesting a potential role in CPA-driven inflammatory responses.

4.7. CPA stimulation in vitro functionally validates the pro-NETotic reprogramming of neutrophils

Given the transcriptional priming of neutrophils for NETs formation observed *in vivo* (Fig. 6), we next sought to determine whether CPA can directly induce NETs release. To address this, we utilized peripheral blood cells from both mice and healthy human donors.

To first obtain direct visual evidence, we stimulated highly purified neutrophils with CPA. Immunofluorescence staining revealed abundant extracellular NETs structures, marked by co-localized MPO and CitH3 in CPA-treated neutrophils from both species (Fig. 7A and B). These NETs appeared as fine fibrous networks extending from the cells, in stark contrast to the PBS-treated neutrophils, which retained a rounded morphology. This fibrous morphology is a hallmark of NETs release and confirms that CPA directly triggers classical NETosis in isolated neutrophils. In addition, as ROS are critical mediators of NETosis, we assessed CPA-induced ROS production. Flow cytometry analysis showed that CPA stimulation led to a significant increase in the level of ROS in neutrophils (Fig. 7C and D).

To enable robust quantitative analyses such as qPCR, which require larger cell numbers, we utilized PBMCs for subsequent experiments. To further evaluate the molecular response, we analyzed the expression of NETs-associated genes by qPCR in CPA-stimulated PBMCs. Remarkably, the gene expression profile mirrored that observed in neutrophils *in vivo*, with significant upregulation of *Tlr4, Padi4, Hmox1, Nfe2l2, and Cybb* (Fig. 7E). This strongly suggests that neutrophils are the primary responders within this mixed cell population. Consistently, Western blot analysis of cell lysates confirmed increased protein levels of PAD4 and CitH3 following CPA treatment (Fig. 7F and G), further supporting enhanced NETs-forming activity.

Finally, to confirm the mode of cell death, we again used flow cytometry on stimulated PBMCs. Analysis of the neutrophil gate revealed that CPA did not trigger Caspase-3 activation or induce a canonical apoptotic phenotype (Annexin V^+/7-AAD^-) in either mouse or human neutrophils (Fig. 7H and I), corroborating our *in vivo* data (Fig. 4I). These data substantiate that NETosis, not apoptosis, is the primary cell death pathway directly induced by CPA.

In summary, our *in vitro* experiments provide direct functional validation for the pro-NETotic signature we identified *in vivo*. By first using purified neutrophils to visually confirm CPA's ability to induce bona fide NETs, and then using peripheral blood leukocytes to quantitatively demonstrate that this process is ROS-dependent, non-apoptotic, and driven by a molecular program identical to that seen *in vivo*, we establish a complete evidentiary chain. These findings confirm that CPA can directly act on neutrophils to execute the NETosis program.

5. Conclusions

This study uncovers a previously unrecognized immunopathological mechanism by which CPA disrupts neutrophil homeostasis and drives pathological NETosis. Through single-cell transcriptomics and functional validation, we characterize a CPA-neutrophil-NETs axis in which CPA mobilizes immature neutrophils from the bone marrow and reprograms them toward a NETs-forming phenotype *via* the TLR4−NOX2−PAD4 signaling cascade. While our findings establish a functional link between CPA exposure and NETosis, pinpointing the direct molecular receptors or intracellular sensors for CPA will be a crucial next step. This will fully elucidate the initial molecular dialogue between the toxin and the neutrophil, potentially revealing a common vulnerability that could be targeted across different toxin-producing pathogens.

Our study demonstrates that CPA-induced NETosis not only leads to neutrophil death but also directly contributes to increased mortality in mice. These findings underscore the critical role of NETs in driving the inflammatory response. However, the pathological relevance of this axis extends beyond immediate tissue damage. Sustained NETs activity is known to trigger a cascade of secondary complications; their web-like structures can promote thrombosis by activating platelets and coagulation factors, cause vascular leakage by disrupting endothelial barriers, and drive organ fibrosis in chronic settings. Thus, the CPA−NETs axis provides a mechanistic framework for understanding how bacterial toxins can initiate these severe, downstream immunopathological events.

Conceptually, this work redefines CPA as not only a cytolytic toxin but also a potent immune modulator that hijacks host defense mechanisms for pathological ends. This insight opens new therapeutic avenues. Our results show that targeting NETosis itself—*via* PAD4 inhibition, extracellular DNA degradation, or neutrophil depletion—markedly reduces tissue damage and improves survival. This highlights NETs as both biomarkers and actionable targets in acute inflammatory syndromes. In the future, these host-directed strategies could be complemented by targeting the trigger itself. The development of CPA-neutralizing antibodies or preventive vaccines represents a highly promising strategy, not only to block the toxin's cytolytic activity but also to preempt the devastating inflammatory cascade it initiates.

In conclusion, our findings suggest that the exploitation of neutrophil plasticity to induce excessive NETosis may be a

generalizable mechanism by which diverse microbial toxins induce immunopathology. The CPA−NETs axis thus provides a valuable model for understanding and therapeutically targeting neutrophil-driven inflammation across a range of infectious and inflammatory disorders, ultimately providing a new playbook for combating a wide array of toxin-mediated diseases by targeting a shared host response.

Acknowledgments

This work was supported by the National Natural Science Foundation of China (No. 82204262, China). The schematic illustration of the graphical abstract was drawn by Figdraw (https://www.figdraw.com).

Author contributions

Pinnan Zhao: Methodology, Data curation, Writing-original draft. Zongcheng Li: Formal analysis, Methodology. Chaoyan Yao: Visualization, Data curation. Visualization, Supervision. Yi Zhou: Validation, Investigation. Yangyihua Zhou: Investigation, Formal analysis. Ning Shi: Validation, Formal analysis. Jie Wang: Formal analysis, Data curation. Can Xu: Methodology, Software. Peixun Gao: Validation, Formal analysis, Investigation. Xuechen Yang: Data curation, Experimental investigation. Liang Zhang: Data collection, Experimental investigation, Validation. Yaowei Ma: Validation, Formal analysis. Jiannan Feng: Investigation. Chunxia Qiao: Conceptualization, Visualization. Xinying Li: Conceptualization, Methodology. Changyan Li: Conceptualization, Supervision. Longlong Luo: Conceptualization, Resources, Funding acquisition, Supervision. Xiang Gao: Conceptualization, Methodology, Writing−review & editing, Supervision.

Conflicts of interest

The authors declare no conflicts of interest.

Appendix A. Supporting information

Supporting information to this article can be found online at https://doi.org/10.1016/j.apsb.2025.09.011.

References

1. Baker RE, Mahmud AS, Miller IF, Rajeev M, Rasambainarivo F, Rice BL, et al. Infectious disease in an era of global change. *Nat Rev Microbiol* 2022;**20**:193−205.
2. Ahuja SK, Manoharan MS, Lee GC, McKinnon LR, Meunier JA, Steri M, et al. Immune resilience despite inflammatory stress promotes longevity and favorable health outcomes including resistance to infection. *Nat Commun* 2023;**14**:3286.
3. Global burden of bacterial antimicrobial resistance 1990-2021: a systematic analysis with forecasts to 2050. *Lancet* 2024;**404**:1199−226.
4. Zhang H, Zhou YL, Qu MD, Yu Y, Chen ZY, Zhu SN, et al. Tissue factor-enriched neutrophil extracellular traps promote immunothrombosis and disease progression in sepsis-induced lung injury. *Front Cell Infect Microbiol* 2021;**11**:677902.
5. Ahmad M, Aduru SV, Smith RP, Zhao Z, Lopatkin AJ. The role of bacterial metabolism in antimicrobial resistance. *Nat Rev Microbiol* 2025;**23**:439−54.
6. Smith WPJ, Wucher BR, Nadell CD, Foster KR. Bacterial defences: mechanisms, evolution and antimicrobial resistance. *Nat Rev Microbiol* 2023;**21**:519−34.
7. Abbas A, Barkhouse A, Hackenberger D, Wright GD. Antibiotic resistance: a key microbial survival mechanism that threatens public health. *Cell Host Microbe* 2024;**32**:837−51.
8. Wang H, Kim SJ, Lei Y, Wang SH, Wang H, Huang H, et al. Neutrophil extracellular traps in homeostasis and disease. *Signal Transduct Targeted Ther* 2024;**9**:235.
9. Kiwit A, Lu Y, Lenz M, Knopf J, Mohr C, Ledermann Y, et al. The dual role of neutrophil extracellular traps (NETs) in sepsis and ischemia−reperfusion injury: comparative analysis across murine models. *Int J Mol Sci* 2024;**25**:3787.
10. Zhou XY, Jin JJ, Lv TF, Song Y. A narrative review: the role of NETs in acute respiratory distress syndrome/acute lung injury. *Int J Mol Sci* 2024;**25**:1464.
11. Cesta MC, Zippoli M, Marsiglia C, Gavioli EM, Cremonesi G, Khan A, et al. Neutrophil activation and neutrophil extracellular traps (NETs) in COVID-19 ARDS and immunothrombosis. *Eur J Immunol* 2023;**53**:e2250010.
12. Bhatia N, George B, Masih D, Khan MMU, Malik P. Mechanistic insights into PAMP and DAMP driven activation of NETosis in autoimmune disorders. *Int Immunopharmacol* 2025;**162**:115149.
13. Mimee M, Citorik RJ, Lu TK. Microbiome therapeutics—advances and challenges. *Adv Drug Deliv Rev* 2016;**105**:44−54.
14. Mehdizadeh Gohari I, M AN, Li J, Shrestha A, Uzal F, B AM. Pathogenicity and virulence of *Clostridium perfringens*. *Virulence* 2021;**12**:723−53.
15. Navarro MA, McClane BA, Uzal FA. Mechanisms of action and cell death associated with *Clostridium perfringens* toxins. *Toxins* 2018;**10**:212.
16. Oda M, Terao Y, Sakurai J, Nagahama M. Membrane-binding mechanism of *Clostridium perfringens* alpha-toxin. *Toxins* 2015;**7**:5268−75.
17. Grenda T, Jarosz A, Sapała M, Grenda A, Patyra E, Kwiatek K. *Clostridium perfringens*-opportunistic foodborne pathogen, its diversity and epidemiological significance. *Pathogens* 2023;**12**:768.
18. Kiu R, Hall LJ. An update on the human and animal enteric pathogen *Clostridium perfringens*. *Emerg Microb Infect* 2018;**7**:141.
19. Moustafa S, Zakaria I, Moustafa A, AboSakaya R, Selim A. Bacteriological and serological investigation of *Clostridium perfringens* in lambs. *Sci Rep* 2022;**12**:19715.
20. Camargo A, Ramírez JD, Kiu R, Hall LJ, Muñoz M. Unveiling the pathogenic mechanisms of *Clostridium perfringens* toxins and virulence factors. *Emerg Microb Infect* 2024;**13**:2341968.
21. Rood JI, Adams V, Lacey J, Lyras D, McClane BA, Melville SB, et al. Expansion of the *Clostridium perfringens* toxin-based typing scheme. *Anaerobe* 2018;**53**:5−10.
22. Goossens E, Verherstraeten S, Valgaeren BR, Pardon B, Timbermont L, Schauvliege S, et al. The c-terminal domain of *Clostridium perfringens* alpha toxin as a vaccine candidate against bovine necrohemorrhagic enteritis. *Vet Res* 2016;**47**:52.
23. Takagishi T, Oda M, Kabura M, Kurosawa M, Tominaga K, Urano S, et al. *Clostridium perfringens* alpha-toxin induces Gm1a clustering and trka phosphorylation in the host cell membrane. *PLoS One* 2015;**10**:e0120497.
24. Zhang T, Wang XH, Li WL, Wang HL, Yan L, Zhao LW, et al. *Clostridium perfringens* α toxin damages the immune function, antioxidant capacity and intestinal health and induces PLCγ1/-AMPK/mTOR pathway-mediated autophagy in broiler chickens. *Heliyon* 2024;**10**:e26114.
25. Muñoz-Planillo R, Kuffa P, Martínez-Colón G, Smith BL, Rajendiran TM, Núñez G. K^+ efflux is the common trigger of NLRP3 inflammasome activation by bacterial toxins and particulate matter. *Immunity* 2013;**38**:1142−53.
26. Mathur A, Kay C, Xue YS, Pandey A, Lee J, Jing WD, et al. *Clostridium perfringens* virulence factors are nonredundant activators of the NLRP3 inflammasome. *EMBO Rep* 2023;**24**:e54600.

27. Jing WD, Pilato JL, Kay C, Feng SY, Tuipulotu DE, Mathur A, et al. Clostridium septicum α-toxin activates the NLRP3 inflammasome by engaging GPI-anchored proteins. *Sci Immunol* 2022;**7**:eabm1803.
28. Abtin A, Jain R, Mitchell AJ, Roediger B, Brzoska AJ, Tikoo S, et al. Perivascular macrophages mediate neutrophil recruitment during bacterial skin infection. *Nat Immunol* 2014;**15**:45−53.
29. Liew PX, Kubes P. The neutrophil's role during health and disease. *Physiol Rev* 2019;**99**:1223−48.
30. Papayannopoulos V. Neutrophil extracellular traps in immunity and disease. *Nat Rev Immunol* 2018;**18**:134−47.
31. Zhu CL, Wang Y, Liu Q, Li HR, Yu CM, Li P, et al. Dysregulation of neutrophil death in sepsis. *Front Immunol* 2022;**13**:963955.
32. Zhu YY, Xia X, He Q, Xiao QA, Wang DC, Huang MR, et al. Diabetes-associated neutrophil NETosis: pathogenesis and interventional target of diabetic complications. *Front Endocrinol* 2023;**14**: 1202463.
33. Retter A, Singer M, Annane D. "The NET effect": neutrophil extracellular traps-a potential key component of the dysregulated host immune response in sepsis. *Crit Care* 2025;**29**:59.
34. Kaplan MJ, Radic M. Neutrophil extracellular traps: double-edged swords of innate immunity. *J Immunol* 2012;**189**:2689−95.
35. Scozzi D, Liao FY, Krupnick AS, Kreisel D, Gelman AE. The role of neutrophil extracellular traps in acute lung injury. *Front Immunol* 2022;**13**:953195.
36. Pieterse E, Rother N, Garsen M, Hofstra JM, Satchell SC, Hoffmann M, et al. Neutrophil extracellular traps drive endothelial-to-mesenchymal transition. *Arterioscler Thromb Vasc Biol* 2017;**37**: 1371−9.
37. Malyala P, Singh M. Endotoxin limits in formulations for preclinical research. *J Pharmacol Sci* 2008;**97**:2041−4.
38. Zhang H, Liu JL, Zhou YL, Qu MD, Wang YHZ, Guo KF, et al. Neutrophil extracellular traps mediate m^6A modification and regulates sepsis-associated acute lung injury by activating ferroptosis in alveolar epithelial cells. *Int J Biol Sci* 2022;**18**:3337−57.
39. Zhang DX, Zhong DN, Ouyang J, He J, Qi YC, Chen W, et al. Microalgae-based oral microcarriers for gut microbiota homeostasis and intestinal protection in cancer radiotherapy. *Nat Commun* 2022; **13**:1413.
40. Ferreira MR, Moreira GM, Cunha CE, Mendonça M, Salvarani FM, Moreira ÂN, et al. Recombinant alpha, beta, and epsilon toxins of *Clostridium perfringens*: production strategies and applications as veterinary vaccines. *Toxins* 2016;**8**:340.
41. Lobstein J, Emrich CA, Jeans C, Faulkner M, Riggs P, Berkmen M. SHuffle, a novel *Escherichia coli* protein expression strain capable of correctly folding disulfide bonded proteins in its cytoplasm. *Microb Cell Fact* 2012;**11**:56.
42. Yang SC, Tsai YF, Pan YL, Hwang TL. Understanding the role of neutrophils in acute respiratory distress syndrome. *Biomed J* 2021;**44**: 439−46.
43. Yang T, Xiang CG, Wang XH, Li QQ, Lei SY, Zhang KR, et al. RIPK1 inhibitor ameliorates pulmonary injury by modulating the function of neutrophils and vascular endothelial cells. *Cell Death Discov* 2024;**10**: 152.
44. Yuan JY, Guo L, Ma JT, Zhang HJ, Xiao MX, Li N, et al. HMGB1 as an extracellular pro-inflammatory cytokine: implications for drug-induced organic damage. *Cell Biol Toxicol* 2024;**40**:55.
45. Zhan YQ, Ling YH, Deng QW, Qiu YX, Shen JT, Lai HJ, et al. HMGB1-mediated neutrophil extracellular trap formation exacerbates intestinal ischemia/reperfusion-induced acute lung lnjury. *J Immunol* 2022;**208**:968−78.
46. Qin SX, Wang HC, Yuan RQ, Li H, Ochani M, Ochani K, et al. Role of HMGB1 in apoptosis-mediated sepsis lethality. *J Exp Med* 2006; **203**:1637−42.
47. Kwok AJ, Allcock A, Ferreira RC, Cano-Gamez E, Smee M, Burnham KL, et al. Neutrophils and emergency granulopoiesis drive immune suppression and an extreme response endotype during sepsis. *Nat Immunol* 2023;**24**:767−79.
48. Manz MG, Boettcher S. Emergency granulopoiesis. *Nat Rev Immunol* 2014;**14**:302−14.
49. Mazzoleni V, Zimmermann K, Smirnova A, Tarassov I, Prévost G. *Staphylococcus aureus* Panton-valentine Leukocidin triggers an alternative NETosis process targeting mitochondria. *FASEB J* 2021;**35**: e21167.
50. Poli V, Zanoni I. Neutrophil intrinsic and extrinsic regulation of NETosis in health and disease. *Trends Microbiol* 2023;**31**:280−93.
51. Liu S, Su XL, Pan PH, Zhang LM, Hu YB, Tan HY, et al. Neutrophil extracellular traps are indirectly triggered by lipopolysaccharide and contribute to acute lung injury. *Sci Rep* 2016;**6**:37252.
52. Aghayan AH, Mirazimi Y, Nasehi L, Atashi A. The toxic effects of neutrophil extracellular traps on mesenchymal stem cells. *Mol Biol Rep* 2024;**52**:30.
53. McDonald B, Davis RP, Kim SJ, Tse M, Esmon CT, Kolaczkowska E, et al. Platelets and neutrophil extracellular traps collaborate to promote intravascular coagulation during sepsis in mice. *Blood* 2017;**129**: 1357−67.
54. Deng QF, Pan BH, Alam HB, Liang YJ, Wu ZY, Liu BL, et al. Citrullinated histone H3 as a therapeutic target for endotoxic shock in mice. *Front Immunol* 2019;**10**:2957.
55. Signoretto I, Calzetti F, Finotti G, Lonardi S, Balanzin C, Bianchetto-Aguilera F, et al. Uncovering two neutrophil-committed progenitors that immediately precede promyelocytes during human neutropoiesis. *Cell Mol Immunol* 2025;**22**:316−29.
56. Subramanian V, Knight JS, Parelkar S, Anguish L, Coonrod SA, Kaplan MJ, et al. Design, synthesis, and biological evaluation of tetrazole analogs of Cl-amidine as protein arginine deiminase inhibitors. *J Med Chem* 2015;**58**:1337−44.
57. Chumanevich AA, Causey CP, Knuckley BA, Jones JE, Poudyal D, Chumanevich AP, et al. Suppression of colitis in mice by Cl-amidine: a novel peptidylarginine deiminase inhibitor. *Am J Physiol Gastrointest Liver Physiol* 2011;**300**:G929−38.
58. Montaldo E, Lusito E, Bianchessi V, Caronni N, Scala S, Basso-Ricci L, et al. Cellular and transcriptional dynamics of human neutrophils at steady state and upon stress. *Nat Immunol* 2022;**23**:1470−83.
59. Xie XM, Shi Q, Wu P, Zhang XY, Kambara H, Su JY, et al. Single-cell transcriptome profiling reveals neutrophil heterogeneity in homeostasis and infection. *Nat Immunol* 2020;**21**:1119−33.
60. Pan X, Niu XY, Li YP, Yao YP, Han LR. Preventive mechanism of lycopene on intestinal toxicity caused by cyclophosphamide chemotherapy in mice by regulating TLR4−MyD88/TRIF−TRAF6 signaling pathway and gut−liver axis. *Nutrients* 2022;**14**:4467.
61. Begum R, Thota S, Abdulkadir A, Kaur G, Bagam P, Batra S. NADPH oxidase family proteins: signaling dynamics to disease management. *Cell Mol Immunol* 2022;**19**:660−86.
62. Lewis HD, Liddle J, Coote JE, Atkinson SJ, Barker MD, Bax BD, et al. Inhibition of PAD4 activity is sufficient to disrupt mouse and human NET formation. *Nat Chem Biol* 2015;**11**:189−91.
63. Zhu WN, Ma CH, Ruan J, Zhou FQ, Zhang YJ, Long HY. Alleviating ulcerative colitis with Baitouweng decoction through *Nrf2/HO-1* pathway activation and HMGB1 downregulation. *Chin Pharmacol Bull* 2025;**41**:186−92.